Six More Ultra-faint Milky Way Companions Discovered in the DECam Local Volume Exploration Survey

W. Cerny[1,2,3], C. E. Martínez-Vázquez[4], A. Drlica-Wagner[1,2,5], A. B. Pace[6], B. Mutlu-Pakdil[7], T. S. Li[8],
A. H. Riley[9,10,11], D. Crnojević[12], C. R. Bom[13], J. A. Carballo-Bello[14], J. L. Carlin[15], A. Chiti[1,2], Y. Choi[16],
M. L. M. Collins[17], E Darragh-Ford[18,19,20], P. S. Ferguson[21], M. Geha[3], D. Martínez-Delgado[22], P. Massana[23],
S. Mau[18,19], G. E. Medina[24], R. R. Muñoz[25], E. O. Nadler[26,27], N. E. D. Noël[17], K. A. G. Olsen[28], A. Pieres[29,30],
J. D. Sakowska[17], J. D. Simon[26], G. S. Stringfellow[31], E. J. Tollerud[32], A. K. Vivas[33], A. R. Walker[33], and
R. H. Wechsler[18,19,20]
(DELVE Collaboration)

[1] Kavli Institute for Cosmological Physics, University of Chicago, Chicago, IL 60637, USA; william.cerny@yale.edu
[2] Department of Astronomy and Astrophysics, University of Chicago, Chicago IL 60637, USA
[3] Department of Astronomy, Yale University, New Haven, CT 06520, USA
[4] Gemini Observatory, NSF's NOIRLab, 670 N. A'ohoku Place, Hilo, HI 96720, USA
[5] Fermi National Accelerator Laboratory, P.O. Box 500, Batavia, IL 60510, USA
[6] McWilliams Center for Cosmology, Carnegie Mellon University, 5000 Forbes Avenue, Pittsburgh, PA 15213, USA
[7] Department of Physics and Astronomy, Dartmouth College, Hanover, NH 03755, USA
[8] Department of Astronomy and Astrophysics, University of Toronto, 50 St. George Street, Toronto ON, M5S 3H4, Canada
[9] Institute for Computational Cosmology, Department of Physics, Durham University, South Road, Durham DH1 3LE, UK
[10] George P. and Cynthia Woods Mitchell Institute for Fundamental Physics and Astronomy, Texas A&M University, College Station, TX 77843, USA
[11] Department of Physics and Astronomy, Texas A&M University, College Station, TX 77843, USA
[12] Department of Chemistry and Physics, University of Tampa, 401 West Kennedy Boulevard, Tampa, FL 33606, USA
[13] Centro Brasileiro de Pesquisas Físicas, Rua Dr. Xavier Sigaud 150, 22290-180 Rio de Janeiro, RJ, Brazil
[14] Instituto de Alta Investigación, Sede Esmeralda, Universidad de Tarapacá, Av. Luis Emilio Recabarren 2477, Iquique, Chile
[15] Rubin Observatory/AURA, 950 North Cherry Avenue, Tucson, AZ 85719, USA
[16] Department of Astronomy, University of California, Berkeley, Berkeley, CA 94720, USA
[17] Department of Physics, University of Surrey, Guildford GU2 7XH, UK
[18] Department of Physics, Stanford University, 382 Via Pueblo Mall, Stanford, CA 94305, USA
[19] Kavli Institute for Particle Astrophysics & Cosmology, P.O. Box 2450, Stanford University, Stanford, CA 94305, USA
[20] SLAC National Accelerator Laboratory, Menlo Park, CA 94025, USA
[21] Department of Physics, University of Wisconsin-Madison, Madison, WI 53706, USA
[22] Instituto de Astrofísica de Andalucía, CSIC, E-18080 Granada, Spain
[23] Department of Physics, Montana State University, P.O. Box 173840, Bozeman, MT 59717-3840, USA
[24] Astronomisches Rechen-Institut, Zentrum für Astronomie der Universität Heidelberg, Mönchhofstr. 12-14, D-69120 Heidelberg, Germany
[25] Departamento de Astronomía, Universidad de Chile, Camino El Observatorio 1515, Las Condes, Santiago, Chile
[26] Observatories of the Carnegie Institution for Science, 813 Santa Barbara Street, Pasadena, CA 91101, USA
[27] Department of Physics & Astronomy, University of Southern California, Los Angeles, CA 90007, USA
[28] NSF's National Optical-Infrared Astronomy Research Laboratory, 950 N. Cherry Avenue, Tucson, AZ 85719, USA
[29] Laboratório Interinstitucional de e-Astronomia—LIneA, Rua Gal. José Cristino 77, Rio de Janeiro, RJ—20921-400, Brazil
[30] Observatório Nacional, Rua Gal. José Cristino 77, Rio de Janeiro, RJ—20921-400, Brazil
[31] Center for Astrophysics and Space Astronomy, University of Colorado, 389 UCB, Boulder, CO 80309-0389, USA
[32] Space Telescope Science Institute, 3700 San Martin Drive, Baltimore, MD 21218, USA
[33] Cerro Tololo Inter-American Observatory, NSF's National Optical-Infrared Astronomy Research Laboratory, Casilla 603, La Serena, Chile

Abstract

We report the discovery of six ultra-faint Milky Way satellites identified through matched-filter searches conducted using Dark Energy Camera (DECam) data processed as part of the second data release of the DECam Local Volume Exploration (DELVE) survey. Leveraging deep Gemini/GMOS-N imaging (for four candidates) as well as follow-up DECam imaging (for two candidates), we characterize the morphologies and stellar populations of these systems. We find that these candidates all share faint absolute magnitudes ($M_V \geqslant -3.2$ mag) and old, metal-poor stellar populations ($\tau > 10$ Gyr, [Fe/H] < -1.4 dex). Three of these systems are more extended ($r_{1/2} > 15$ pc), while the other three are compact ($r_{1/2} < 10$ pc). From these properties, we infer that the former three systems (Boötes V, Leo Minor I, and Virgo II) are consistent with ultra-faint dwarf galaxy classifications, whereas the latter three (DELVE 3, DELVE 4, and DELVE 5) are likely ultra-faint star clusters. Using data from the Gaia satellite, we confidently measure the proper motion of Boötes V, Leo Minor I, and DELVE 4, and tentatively detect a proper-motion signal from DELVE 3 and DELVE 5; no signal is detected for Virgo II. We use these measurements to explore possible associations between the newly discovered systems and the Sagittarius dwarf spheroidal, the Magellanic Clouds, and the Vast Polar Structure, finding several plausible associations. Our results offer a preview of the numerous

ultra-faint stellar systems that will soon be discovered by the Vera C. Rubin Observatory and highlight the challenges of classifying the faintest stellar systems.

Unified Astronomy Thesaurus concepts: Star clusters (1567); Dwarf galaxies (416); Sky surveys (1464)

1. Introduction

The standard picture of galaxy formation within the Lambda cold dark matter paradigm describes that galaxies form from the condensation of gas onto dark matter "halos," which grow over cosmic time through merging and accretion of lower-mass "subhalos" (e.g., White & Rees 1978; Blumenthal et al. 1984; Jenkins et al. 2001; Springel et al. 2008; Kravtsov 2010). As a result of this hierarchical formation channel, the dark matter halos hosting massive galaxies like the Milky Way are expected to be rich with substructure, boasting numerous subhalos, which can host their own small galaxies (e.g., Diemand et al. 2007; Springel et al. 2008; Kravtsov 2010; Griffen et al. 2016). The least-massive and least-luminous galaxies in this hierarchy are known as "ultra-faint" dwarf galaxies (see Simon 2019 for a recent review). These extreme systems are believed to have originated within some of the earliest halos to collapse in the universe, and likely formed multiple generations of stars quickly before being quenched during or before the epoch of reionization (Brown et al. 2014; Sacchi et al. 2021). The dark matter halos that host these galaxies provided sufficiently deep gravitational potential wells to retain ejecta from supernovae, and, by virtue of their resident galaxies' lack of extended star formation, preserve a fossil record of their chemical enrichment histories (Bovill & Ricotti 2009; Willman & Strader 2012; Frebel & Bromm 2012). This formation and evolutionary pathway makes these galaxies nearly pristine laboratories for studying the nature of dark matter, tracing the births and deaths of the first stars, and studying the physics of the early universe.

Although ultra-faint dwarf galaxies are expected to be the most numerous class of galaxy in the universe, their diffuse morphologies and exceedingly low luminosities rendered them undetectable until relatively recently. It was not until the advent of the Sloan Digital Sky Survey (SDSS; York et al. 2000) and the application of automated matched-filter search algorithms that the first exemplar of these systems was detected (Willman et al. 2005). Since these early efforts in SDSS, numerous deep, wide-area surveys including the Panoramic Survey Telescope and Rapid Response System 1 survey (PS1; Chambers et al. 2016), the VLT Survey Telescope ATLAS survey (Shanks et al. 2015), the Dark Energy Survey (DES; DES Collaboration 2005), the Hyper Suprime-Cam Subaru Strategic Program survey (HSC SSP; Aihara et al. 2018), and the DECam Local Volume Exploration survey (DELVE; Drlica-Wagner et al. 2020) have enabled the rapid discovery of ultra-faint galaxies around the Milky Way. Recently, the European Space Agency Gaia satellite has also offered the ability to detect comoving structures in the stellar halo, expanding the detectable parameter space of dwarf galaxies to larger physical sizes and lower surface brightness thresholds (Torrealba et al. 2019b; Darragh-Ford et al. 2021). The census of ultra-faint dwarf galaxies has now advanced to more than 60 systems, nearly all of which have been identified as resolved satellites of the Milky Way, M31/Andromeda, and a select few nearby hosts in the Local Volume (McConnachie 2012; Simon 2019, and references therein). These systems continue to be discovered at a rapid pace, with roughly 10 ultra-faint dwarf galaxy candidates discovered in the last few years alone (e.g., see Homma et al. 2019; Mau et al. 2020; Cerny et al. 2021a, 2023; Martínez-Delgado et al. 2022; Mutlu-Pakdil et al. 2022; Collins et al. 2022; Sand et al. 2022; Bell et al. 2022).

In tandem with recent dwarf galaxy discoveries, systematic searches for ultra-faint systems have also uncovered an enigmatic population of faint, compact, and ancient stellar systems with absolute magnitudes $M_V \gtrsim -3$, azimuthally averaged half-light radii $r_{1/2} < 15$ pc, and heliocentric distances $D_\odot > 10$ kpc (e.g., Fadely et al. 2011; Muñoz et al. 2012; Balbinot et al. 2013; Koposov et al. 2017; Torrealba et al. 2019a; Mau et al. 2020). These systems have typically been classified as ultra-faint halo star clusters on the basis of their lower luminosities, smaller sizes, and more spherical stellar density distributions relative to the known population of ultra-faint dwarf galaxies. Under this interpretation, these systems may have originated within low-mass galaxies that disrupted while accreting onto the Milky Way, as is believed to be the case for at least some of the Milky Way's "classical" globular clusters (Searle & Zinn 1978). Although these systems likely do not exhibit the high dark matter densities and mass-to-light ratios of their dwarf galaxy counterparts, many of these clusters may have nonetheless survived the strong tidal forces exerted on them by the Milky Way by virtue of their compactness. This all being said, the relatively small number of known ultra-faint halo star clusters, combined with the near-complete lack of spectroscopic radial velocity and velocity dispersion measurements for these systems, has limited our ability to assess both their dark matter contents and their origins.

Here, we present the discovery of six ultra-faint Milky Way satellite systems spanning an intermediate range of physical sizes encompassing both the star cluster and dwarf galaxy regimes. In Section 2, we present an overview of the DELVE DR2 data set and our satellite search procedure. In Section 3, we describe our follow-up imaging of these candidates using the Gemini Multi-Object Spectrograph at Gemini North (GMOS-N) and the Dark Energy Camera (DECam). We use this imaging data to characterize the morphologies and stellar populations of these systems in Section 4, as well as measure their proper motions using data from the Gaia satellite. In Section 5 and Section 6, we discuss the nature and classifications of these individual systems and their potential associations with various Local Group structures. We conclude in Section 7.

2. DELVE Data and Satellite Search

2.1. DELVE DR2

We conducted a search for arcminute-scale stellar substructures in the Milky Way halo using data from the second data release of DELVE (DELVE DR2; Drlica-Wagner et al. 2022).[34] DELVE seeks to achieve contiguous, multiband coverage of the entire high-Galactic-latitude sky accessible to DECam (Flaugher et al. 2010) by combining 126 nights of new DECam observations in the g, r, i, and z bands with existing archival data from numerous NOIRLab community programs.

---

[34] https://datalab.noirlab.edu/delve/

DELVE processes all exposures with the Dark Energy Survey Data Management pipeline (Morganson et al. 2018), and derives astrometric and photometric measurements from individual exposures, as opposed to making measurements on stacked images. The catalogs from the individual exposures are matched across filters and merged to form a single unified multiband catalog following the procedure described in Drlica-Wagner et al. (2020).

The most recent iteration of the DELVE photometric catalog, DELVE DR2, was derived from ∼160,000 exposures spanning a sky area of 20,000–25,000 $\deg^2$ in each band, with >17,000 $\deg^2$ of simultaneous four-band coverage. The DECam programs contributing the largest number of exposures to DELVE DR2 include DELVE itself (Proposal ID: 2019A-0305), DES (DES Collaboration et al. 2021), the DECam Legacy Surveys (DECaLS; Dey et al. 2019), and the DECam eROSITA Survey (DeROSITAS; Proposal ID: 2021A-0149). As depicted for the g band in Figure 1, the full DELVE DR2 data set spans nearly the entire southern sky with Galactic latitude $|b| > 10°$ and decl. $\delta_{2000} < 0°$, as well as ∼2/3 of the sky above the celestial equator with $|b| > 10°$ and $\delta_{2000} \lesssim 33°$; we note that this includes the full footprint of DELVE DR1 and DES DR2. The median 10σ point-source depths for DELVE DR2 are $g = 23.5$, $r = 23.1$, $i = 22.7$, and $z = 22.1$ mag, although these vary as a function of sky position depending on the available archival data. We refer the reader to Drlica-Wagner et al. (2020) and Drlica-Wagner et al. (2022) for a more complete description of the DELVE science goals, observing strategy, data processing pipeline, and data products.

We corrected the DELVE DR2 photometry, as well as all other photometry presented in this work, for reddening due to interstellar dust by interpolating the $E(B-V)$ values from the maps of Schlegel et al. (1998) with the rescaling from Schlafly & Finkbeiner (2011). We then calculated bandpass-specific extinctions using the total-to-selective absorption coefficients from DES DR1 (DES Collaboration et al. 2018). Throughout this work, all reported magnitudes refer to AB magnitudes in the DECam photometric system unless otherwise noted, with extinction-corrected magnitudes denoted by a subscript "0."

2.2. Satellite Search

Our satellite search consisted of running four iterations of the `simple` algorithm, which has previously been applied to data from multiple DECam survey programs, as well as data from PS1, to conduct an extensive census of Milky Way satellites (Bechtol et al. 2015; Drlica-Wagner et al. 2015, 2020).[35] The `simple` algorithm applies an isochrone matched-filter in color–magnitude space defined by two filter bands to enhance the density contrast of halo substructures across a range of distances.

We began by dividing the DELVE DR2 footprint into HEALPix (Górski et al. 2005) pixels at NSIDE = 32, corresponding to an area of 3.4 $\deg^2$. We then selected all stars with colors consistent with a synthetic Bressan et al. (2012) isochrone, which was scanned across a grid of distance moduli spanning $(m - M)_0 = 18.0$ to $(m - M)_0 = 21.5$ in steps of 0.25 mag (corresponding to ∼40 kpc to 200 kpc). Next, the resulting stellar density field was filtered with a Gaussian kernel ($\sigma = 2'$), and local overdensities were identified by iteratively raising a density threshold until fewer than 10 disconnected peaks remained. Each overdensity was assigned a

significance based on the Poisson significance of the observed stellar counts compared to the field density estimated from a concentric background annulus.

To maximize the discovery potential of the search, we specifically ran four iterations of the procedure above. Two of these iterations ran over all regions of DELVE DR2 with simultaneous g, r band coverage, while the other two covered regions with g, i band data. For each filter pair, we performed a single search using an old, metal-poor PARSEC isochrone (Bressan et al. 2012) with $\tau = 12$ Gyr; $Z = 0.0001$ ([Fe/H] ∼ −2.2 dex) and another with a slightly more metal-rich isochrone with $\tau = 12$ Gyr; $Z = 0.0005$ ([Fe/H] ∼ −1.5 dex). These searches individually produced thousands of overdensities above our nominal significance threshold of 5.5σ. We proceeded to generate diagnostic plots for this composite sample of overdensities, from which we identified 54 that merited further investigation on the basis of their smoothed stellar density distributions (as in Figure 1), color–magnitude diagrams, or appearance in the color images available through the Legacy Surveys Sky Viewer (see Section 5 for more details). Many of these 54 overdensities were independently detected across two or more iterations of our search (e.g., in the g, r search and the g, i search), suggesting that the signals at these locations were robust to at least some of our search systematics. We did not require overdensities to be detected in multiple iterations of our search because the sky regions covered by the r and i bands differ considerably. Nonetheless, the final six candidates that we report were each detected in ⩾2 of the search iterations (see Section 5). In addition to these 54 overdensities, we also reidentified a large number of previously reported systems, including, for example, all of those discovered in earlier searches of the DELVE data (Mau et al. 2020; Cerny et al. 2021a, 2021b, 2023).

We ran a full Markov Chain Monte Carlo (MCMC) parameter fit to the structure and stellar population of all 54 overdensities using the Ultra-faint GALaxy LIkelihood software toolkit (`ugali`; see Section 4.2). For a significant majority of these systems, the MCMC failed to converge or converged to a clearly nonphysical outcome.[36] This allowed us to further narrow the sample to seven candidates, which we believed to be genuine stellar associations in the Milky Way halo (i.e., dwarf galaxies or star clusters). We were able to acquire deeper follow-up data for six of these systems, which form the basis of this work. We were unable to constrain the properties of the seventh candidate system given the shallow depth of the available data, and we intend to revisit it at a later date when follow-up observations become available.

Figure 1 shows the spatial distribution of the candidates reported in this work (red dots), overlaid on the DELVE DR2 g-band footprint (light blue). Although we do not seek to quantify our search sensitivity and completeness in this paper, we do observe that five of our six candidates lie in regions of sky at $\delta_{2000} > 0°$ covered by DECaLS. There are at least two possible interpretations of the spatial distribution of our candidates. First, DELVE has already reported four satellite systems south of the equator and one in the north at $\alpha_{2000} \sim 330°$; by consequence of these previous searches, subsequent discoveries in DELVE are less likely to fall in

---

[35] https://github.com/DarkEnergySurvey/simple

---

[36] Most often, the failure involved the MCMC converging to the maximum size allowed by our prior bounds. Because the small kernel size used in the search was specifically chosen to detect compact (arcminute-scale) overdensities, these cases could safely be rejected as false-positive detections.
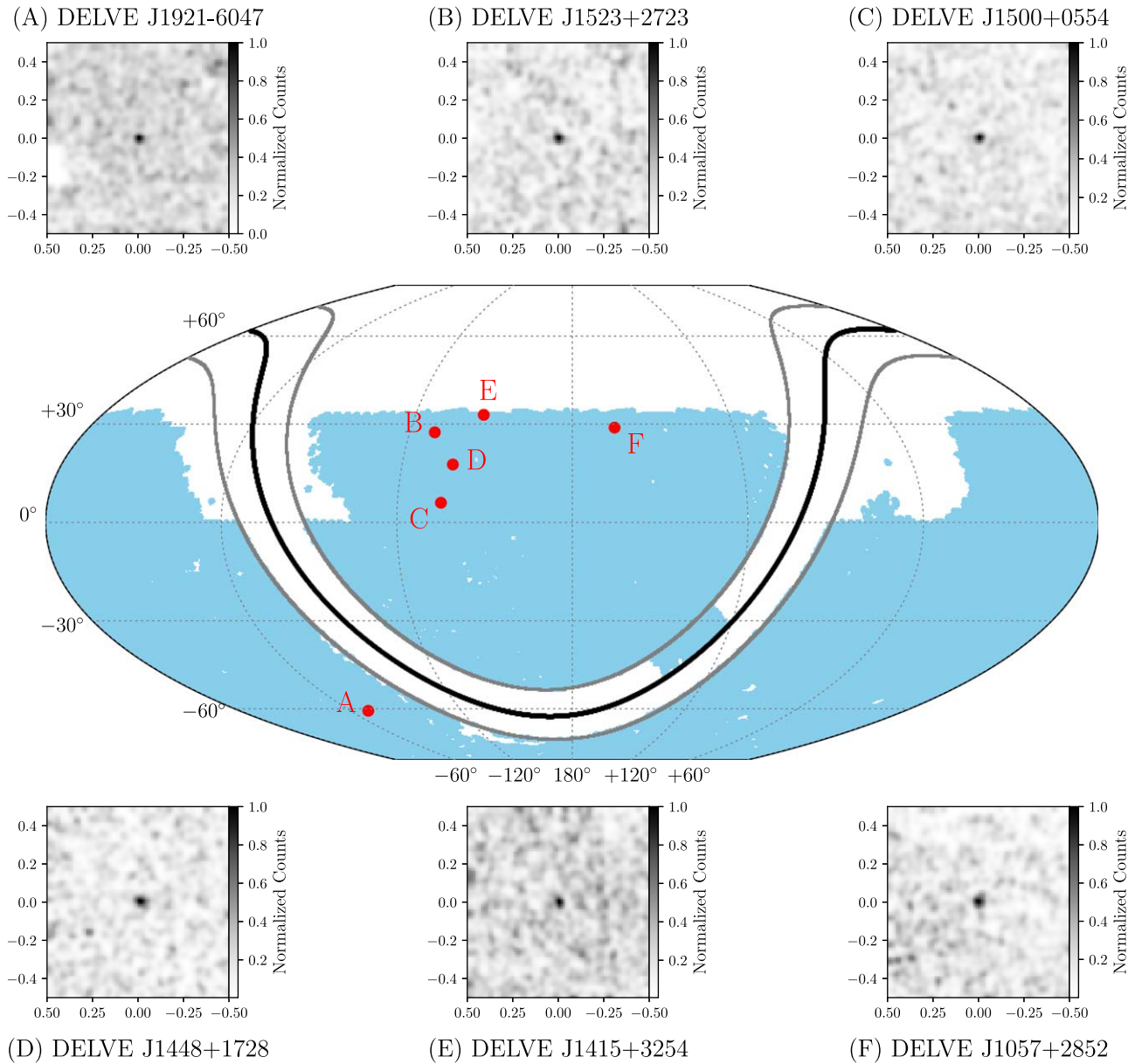
(A) DELVE J1921-6047

(B) DELVE J1523+2723

(C) DELVE J1500+0554

(D) DELVE J1448+1728

(E) DELVE J1415+3254

(F) DELVE J1057+2852

Figure 1. Skymap of the DELVE DR2 g-band coverage (blue background), shown in McBryde-Thomas flat-polar quartic projection. The Galactic plane ($b = 0°$) is shown as a solid black curve, and two curves denoting $b = \pm 10°$ are shown in gray. The locations of the candidates reported in this work are shown as red dots, labeled by decreasing R.A. Each inset panel shows the isochrone-filtered stellar density field for a $1°\!.0 \times 1°\!.0$ region centered on a given candidate, smoothed with a $1'$ Gaussian kernel. These panels were generated exclusively using DELVE DR2 data, and do not include the follow-up exposures from DECam and GMOS-N described in Section 3. These panels include only sources with g_0, $r_0 < 24$ mag and with $0 \leqslant$ EXTENDED_CLASS_G $\leqslant 2$ (see Drlica-Wagner et al. 2022 for details on this morphological classifier).

those regions. Second, the Legacy Surveys Sky Viewer made it possible to quickly inspect color images of each candidate in these regions, which proved especially useful for assessing the presence of compact stellar systems; a similar tool is not yet available for DECam data in the south outside of DES. The final candidate falls just outside of the DES footprint, suggesting that additional candidates may yet be discovered even in previously inspected regions of the DELVE survey. On that note, we emphasize that our goal in this work is not to provide a comprehensive census of all Milky Way satellites in DELVE DR2 footprint, but to instead present a sample of candidates for which we have a high degree of confidence and for which we were able to obtain follow-up data. We intend to quantify the detection completeness of our satellite searches at

a later date when deeper photometry over the DELVE area based on image-level coaddition becomes available.

During the preparation of this manuscript, the authors of Smith et al. (2022) informed us of their independent discovery of the stellar system referred to here as Boötes V using data from the Ultraviolet Near-Infrared Optical Northern Survey (UNIONS).[37] We have not altered our analysis of this system in light of their work, nor have we reviewed their manuscript. We also note that this system, as well as the system that we name DELVE 4, is included in the candidate lists from Darragh-Ford et al. (2021), who identified this system by applying a wavelet transform approach to Gaia proper-motion

---

[37] https://www.skysurvey.cc/

Table 1
Summary of Follow-up Observations Presented in This Work

Candidate	Instrument	Exposure Times	Dates	Adopted Magnitude Limit
DELVE J1921-6047 (DELVE 3)	DECam	(g) 3 $\times$ 300 s (r) 3 $\times$ 300 s	2022-07-28	$g_0 = 23.5; r_0 = 23.1$
DELVE J1523+2723 (DELVE 4)	GMOS-N	(g) 5 $\times$ 300 s ; (r) 4 $\times$ 300 s	2022-07-04	$g_0 = 25.09; r_0 = 24.69$
DELVE J1500+0554 (Virgo II)	GMOS-N	(g) 12 $\times$ 150s; (r) 10 $\times$ 150 s	2022-07-20	$g_0 = 26.30; r_0 = 25.79$
DELVE J1448+1728 (DELVE 5)	GMOS-N	(g) 10 $\times$ 300 s ; (r) 3 $\times$ 300 s	2022-07-31	$g_0 = 25.20; r_0 = 24.69$
DELVE J1415+3254 (Boötes V)	GMOS-N	(g) 8 $\times$ 300 s ; (r) 5 $\times$ 350 s	2022-06-27	$g_0 = 25.87; r_0 = 25.51$
DELVE J1057+2852 (Leo Minor I)	DECam	(g) 3 $\times$ 300s; (r) 3 $\times$ 300 s	2022-05-21	$g_0 = 23.4; r_0 = 23.1$

Note. The DECam exposures reported here represent only the follow-up exposures that we collected; however, these were combined with existing archival observations to generate the catalog we used throughout this work. For the candidates with GMOS-N data, this table reports only the exposures that ultimately became part of our photometric catalogs, and therefore excludes some exposures with lower image quality that were taken as part of our program (especially g-band exposures targeting DELVE 4). We note that additional r-band observations of DELVE 5 were planned but not executed due to Gemini queue constraints. The DECam magnitude limits correspond to the 10σ depth and the GMOS-N magnitude limits corresponding to the 30% completeness level based on the artificial star tests described in Section 3.1.

data; however, the authors did not specifically isolate these systems for study. We encourage the reader to review these works for details about these complementary search efforts.

3. Follow-up Imaging of the Newly Discovered Candidates with DECam and Gemini/GMOS-N

We pursued deeper follow-up imaging of each newly discovered candidate with either DECam on the 4-m Blanco Telescope or GMOS-N (Davies et al. 1997; Hook et al. 2004) on the 8.1-m Gemini North Telescope during late spring and summer of 2022. The goal of these observations was to increase the number of putative member stars in each system in order to confirm whether they represented bona fide associations of stars, and, if so, to improve constraints on their stellar populations and structural properties.

In brief, this follow-up imaging consisted of (1) a 4 hr Gemini Fast Turnaround program targeting DELVE J1523+2723, DELVE J1500+0554, and DELVE J1148+1728, (2) a 1.4 hr Gemini Director's Discretionary program studying DELVE J1415 +3254, (3) 30 minutes of DECam imaging targeting DELVE J1057+2852 during regular DELVE observing time, and (4) 30 minutes of DECam imaging targeting DELVE 1921-6047, again during regular DELVE time. A summary of these observations is presented in Table 1. We describe the corresponding data reduction procedures in the following sections.

3.1. GMOS-N Data Reduction and Photometry

We reduced the GMOS-N data using a lightly modified version of the standard GMOS-N imaging reduction pipeline implemented by the Data Reduction for Astronomy from Gemini Observatory North and South platform (DRAGONS; Labrie et al. 2019).[38] The DRAGONS recipe for GMOS-N image reduction automatically performs overscan and bias subtraction, flat-fielding, image stacking, and cosmic-ray rejection based on the stacked image. Because Gemini operates on a queue, we did not collect our own flat and bias frames; instead, we used the most recently available flat and bias frames in the Gemini archive.

We performed point-spread function (PSF) photometry on the resultant g and r stacked images using the DAOPHOT IV/ ALLSTAR suite of codes (Stetson 1987). An empirical PSF was derived for each image using ~50 stars that were not saturated,

far from the edges of the CCDs, and spread over the whole field of view (FOV). A Moffat function ($\beta = 2.5$) was the preferred PSF model over the whole set of images since it provided the smallest residuals. Following the same procedure as in Martínez-Vázquez et al. (2021), we performed initial photometry on the stacked images with a spatially constant PSF using ALLSTAR; this provided both a preliminary photometric catalog and a star-subtracted image. Because some of the faintest sources were undetected in this first pass, we identified these faint sources using the star-subtracted image and appended them to our previous catalog in order to obtain a more complete catalog for every image. This strategy enables the recovery of faint sources located in the PSF wings of brighter objects (e.g., Martínez-Vázquez et al. 2021; Cantu et al. 2021). Finally, after subtracting the PSF stars from the stacked images, we refined the PSF model and also allowed a quadratic variation of the PSF throughout the FOV in order to perform the final PSF photometry for our catalog.

We then calibrated the instrumental GMOS-N photometry into the DECam photometric system using the available data from DELVE DR2, including a color term to account for the difference between the DECam and GMOS-N filter systems. We explored a range of calibration techniques, and found that deriving the color term from the photometry for a given candidate provided a better relative calibration than a simultaneous fit to the photometry for all four candidates with GMOS-N data; however, no solution was found to be perfect. To account for lingering differences between the DELVE DR2 photometry and the calibrated GMOS-N photometry, we assume a 0.03 mag photometric error floor for all GMOS-N magnitudes quoted in this work. This primarily affects a small number of brighter stars in each candidate, as the photometric errors for fainter sources are dominated by photon shot noise (as quantified via the artificial star tests described below).

To determine the completeness and photometric errors of our GMOS-N data as a function of magnitude, we performed artificial star tests following a similar approach to that described in Monelli et al. (2010). Approximately 30,000 artificial stars were injected into each stacked GMOS-N image spread over a regular grid covering the FOV. Artificial stars were placed at the vertices of equilateral triangles separated by a distance of twice the PSF radius plus one pixel. This strategy allowed us to add the artificial stars in a way that avoids overcrowding. Depending on the image quality of each stacked image, we injected between 1160 and 1900 artificial stars per

---

[38] https://dragons.readthedocs.io/en/stable/

iteration and per filter, for 16–25 iterations. The colors and magnitudes of the artificial stars were obtained using IAC-BaSTI synthetic color–magnitude diagrams (Hidalgo et al. 2018; Pietrinferni et al. 2021)[39] and covered the full range of our observed color–magnitude diagrams.

We display the completeness as a function of magnitude in Appendix A, and we report the magnitude corresponding to the 30% completeness limit in Table 1. These values were calculated after making the same photometric quality cuts used in our isochrone-fitting and structural property analyses (see Section 4). We opted to extend our stellar selection to the 30% completeness limit when fitting the distance and structure of the systems observed by GMOS-N to ensure sufficient contrast relative to the background for these faint systems. When deriving the absolute magnitude of each system, we applied a more elaborate completeness correction as a function of magnitude (see Section 4.1.4).

3.2. Additional Exposures from DECam

We collected additional 300 s exposures for DELVE J1057 +2852 and DELVE J1921-6047 with DECam in late 2022 May and 2022 August, respectively. Because of the large decl. of DELVE J1057+2852, we were only able to observe it at airmass ~ 1.9. In conjunction with the poor sky conditions, this conspired to make the new observations comparable in quality to the existing data in DELVE DR2. These observations did, however, fill in the CCD gaps in the g-band coverage from DELVE DR2 (see Figure 1). Although we were able to observe DELVE J1921-6047 at low airmass, the variable sky conditions likewise limited our data quality in the g band. By contrast, a brief window of clear sky allowed us to improve upon the existing r-band data for this system.

We combined these follow-up exposures with the exposures available at the time of discovery to construct new multiband source catalogs following the identical procedure used to generate DELVE DR2. For the analyses described hereafter, we opted to use PSF magnitudes derived from a weighted-average of measurements derived from individual exposures (WAVG_MAG_PSF_G and WAVG_MAG_PSF_R; see Appendix A of DES Collaboration et al. 2021 for details). This allowed us to leverage our follow-up exposures to achieve better photometric precision even in cases where these exposures did not improve upon the seeing or the effective exposure time of the discovery data. In practice, this contributed to slightly better depth for our final catalog compared to DELVE DR2.

4. Properties of the Newly Discovered Systems

We constrained the morphological and stellar population properties of the six candidates through maximum-likelihood analyses using the GMOS-N data (for DELVE J1523+2723, DELVE J1500+0554, DELVE J1448+1728, and DELVE J1057+2852) and the deeper DECam data (for DELVE J1921-6047 and DELVE J1057+2852). Although previous DELVE analyses—all of which have been based on DECam data—have exclusively used the ugali toolkit to characterize the structure and stellar populations of ultra-faint stellar system candidates, the smaller size of the GMOS-N FOV ($5'.5 \times 5'.5$) demanded that we adopt a different approach. More specifically, the smaller GMOS-N FOV would make it difficult to define a

suitably large background annulus to define a foreground model for the ugali joint fit of color, magnitude, and spatial distributions. Therefore, we used ugali only for the candidates with DECam data, and describe our alternate procedure for fitting the candidates with GMOS-N data below.

4.1. Gemini/GMOS-N Analysis

To fit the structural properties of the candidates with GMOS-N imaging, we applied a lightly modified version of the dwarf galaxy structural fitting code presented by Simon et al. (2021),[40] which is a binned Poisson maximum-likelihood procedure based on the formalism presented in Appendix C of Drlica-Wagner et al. (2020). Broadly, the parameter estimation procedure involved three main steps for each candidate: (1) creating a binned coverage mask defining the imaged area, (2) selecting a sample of probable member stars based on a simplified isochrone-fitting procedure, and (3) performing MCMC sampling to describe the posterior probability distribution of the structural parameters assuming a binned Poisson likelihood function. We elaborate upon each of these steps in the subsections below.

4.1.1. Coverage Mask Definition

For each candidate, we began by defining a full-resolution coverage map based on the stacked GMOS-N g-band image produced by DRAGONS. Image pixels within the imaging region of the frame were assigned a value of one, and regions of the focal plane not used for imaging were assigned zero; we found these regions were naturally separated by a threshold pixel value between 500 and 1400 electron counts, depending on the image. Next, we visually identified bright stars and the largest extended galaxies in the image and used a Python implementation of SEextractor, SEP (Barbary 2016), to define isophotal shape and orientation parameters, which we used to mask these objects. We then binned this full-resolution mask into 25×25 pixel bins, assigning a coverage fraction between 0 and 1 representing the number of pixels in each bin that contained a value of one in the full-resolution mask. This represents a divergence from the procedure of Simon et al. (2021), who used a binary (0 or 1) coverage map for their higher-resolution Hubble Space Telescope data.

4.1.2. Distance

We performed a simple isochrone-fitting procedure similar to that of Mutlu-Pakdil et al. (2018) to measure the distance to each candidate. We began by selecting a stellar sample by applying a cuts on the DAOPHOT indices χ and sharp, namely $\chi < 3$ and $-0.5 \leqslant sharp \leqslant 0.7$. We then applied a spatial selection for a given system based on an initial estimate of its angular half-light radius, specifically taking all stars within a circular selection of $r < 2r_h$. Next, we adjusted the age and metallicity of a PARSEC isochrone to the resulting color–magnitude diagram, adopting an initial estimate of the distance provided by a ugali fit to the DECam discovery data. We found that it was necessary to adjust the age and metallicity by eye due to the imperfect relative calibration, the dearth of red giant branch stars, and the generally large photometric errors at the main-sequence turnoff for each system. We then iterated the isochrone with our chosen age and metallicity through a range of distance moduli spanning ± 0.5 mag about the initial guess in intervals of 0.01 mag. At each

---

step, we counted the number of observed stars in a given candidate with colors consistent with the isochrone according to $\Delta(g - r)_0 < \sqrt{0.07^2 + \sigma_g^2 + \sigma_r^2}$, excluding a small number of foreground stars using the high-quality astrometry provided by Gaia Data Release 3 (DR3; Gaia Collaboration et al. 2021; Lindegren et al. 2021; see Section 4.3 for more details). We report the distance modulus that produced the largest number of stars meeting this selection condition.

To define a statistical uncertainty on the distance modulus, we performed a bootstrap resampling (with replacement) of the observed color–magnitude diagram for each candidate 500 times. For each bootstrap iteration, we repeated the procedure described above, finding the distance modulus that maximized the number of stars passing the isochrone selection. The standard deviation of the distance moduli across the bootstrap iterations was defined as the statistical error on our best-fit distance modulus. Lastly, we added an systematic uncertainty of 0.1 mag in quadrature to account for the systematic uncertainty associated synthetic isochrone modeling (Drlica-Wagner et al. 2015), as well as our choice to fix the age and metallicity during this procedure.

We performed the procedure described above for DELVE J1523+2723, DELVE J1500+0554, and DELVE J1448+1728, but not for DELVE J1415+3254. DELVE J1415+3254 was the only candidate for which we detected an unambiguous blue horizontal branch, which provided an excellent anchor for isochrone fitting. Therefore, we chose to adopt the distance modulus from our initial `ugali` fit to the DECam data for this candidate, which was driven by the blue horizontal branch feature; this is likely to be more accurate than a fit to the horizontal branch in the GMOS-N data due to the imperfect relative calibration discussed in Section 3.1. We then proceeded to select the isochrone age and metallicity by eye, as with the other three systems. We assumed a conservative 0.15 mag overall magnitude uncertainty on this horizontal-branch-based distance. We note that adopting the same distance-fitting procedure as with the other candidates would produce a distance modulus of $(m - M)_0 = 19.86 \pm 0.11$, consistent at the $\sim 1.5\sigma$ level with our quoted result.

4.1.3. Final Member Star Selection and Structural Parameters

To estimate structural parameters for the candidates with GMOS-N imaging, we first constructed a final sample of candidate member stars in each system. Specifically, we defined a stellar selection from each candidate's calibrated photometric catalog by applying the same cuts on χ and *sharp* as for the distance estimation, as well as our completeness cut. We then selected all stars consistent with our best-fit isochrone according to $\Delta(g - r)_0 < \sqrt{0.07^2 + \sigma_g^2 + \sigma_r^2}$, where σ_g and σ_r are the magnitude errors for the g and r bands, which include our GMOS-N photometric error floor of 0.03 mag. Lastly, we once again excluded a small number of foreground stars on the basis of their Gaia parallaxes and/or proper motions; this time, however, we used the updated distances provided by the analysis in the previous section when performing this filtering. All stars identified in the GMOS FOV of each candidate that passed each of these member star selection criteria are colored in blue in the center panels of Figures 3–6. These stars constitute the samples that were used to constrain the candidates' structural properties, as described below.

With both the stellar sample and mask defined, we performed a binned Poisson maximum-likelihood fit (Simon et al. 2021) to

each system assuming a Plummer (1911) stellar density profile. The free parameters for these fits were the number of observed stars, the X and Y centroid coordinates (in pixels), the extension/semimajor axis length (in pixels), the ellipticity ($\epsilon = 1 - \frac{b}{a}$), the position angle (in the image frame), and a background surface density (Σ_b; in stars per 10^6 pixels). Unlike Simon et al. (2021), we found that it was necessary to model the background surface density in order to account for Milky Way contamination that passed the isochrone filter. The only remaining change in our procedure relative to Simon et al. (2021) was that we multiplied the predicted model counts in each bin by the corresponding value in the binned coverage fraction mask that we constructed above, allowing for accurate comparison with the observed binned counts within the likelihood function.

To validate the results derived from this procedure, we tested our ability to recover structural parameters in an unbiased manner by simulating stellar populations at the catalog level and re-running the structural fit using one of the GMOS-N coverage masks. We find that we are able to recover the input structural parameters with appropriately quantified uncertainties, and we discuss these tests in greater detail in Appendix C.1. We also varied the input assumptions for the fit and assessed their impact on each candidate's measured structural properties. These included testing alternate bin sizes, varying the magnitude limit and DAOPHOT parameter cuts used to define the input stellar sample, and masking different subsets of bright stars/galaxies in the full-resolution mask for each system. In general, we found that our results were robust to these choices.

Finally, we converted our results from units of pixels to angular units and transformed our position angle measurement from the image frame to the celestial coordinate frame. Specifically, we transformed the posterior probability distributions derived from the MCMC by applying the `pixel_to_world` and `position_angle` functions within `astropy` (Astropy Collaboration et al. 2013; Price-Whelan et al. 2018). The angular semimajor axis length of each candidate was converted to a physical quantity with an uncertainty by Monte Carlo sampling from both the posterior distributions for the angular extension and distance. Lastly, the azimuthally averaged angular (physical) half-light radius was derived from the angular (physical) semimajor axis length via the relation $r_h = a_h \sqrt{1 - \epsilon}$ ($r_{1/2} = a_{1/2}\sqrt{1 - \epsilon}$).

4.1.4. Absolute Magnitude

To estimate the absolute magnitude of our candidates from the GMOS-N data, we followed a simulation-based procedure similar to that described by Martin et al. (2008). We simulated stellar systems consistent with the isochrone parameters and distance of each system assuming a Chabrier (2003) initial mass function. We applied a completeness correction to the simulated stars using the completeness functions derived from artificial star tests (Section 3.1) to predict the number of stars that would be observable brighter that the 30% completeness limit of our GMOS-N data passing our selections on χ and *sharp*. We adjusted the total stellar mass of each system until the predicted number of observable stars matched the number of member stars returned by our structural parameter fit (Section 4.1.3). This yielded an estimate of the total "richness" of the system (Bechtol et al. 2015; Drlica-Wagner et al. 2020), which was then used to derive the absolute magnitude of each system following the method introduced by Martin et al. (2008), as implemented by `ugali`. Since most of the

Table 2
Morphological, Stellar Population, and Proper-motion Properties of the Newly Discovered Systems

Parameter	Unit	DELVE 3	DELVE 4	Virgo II	DELVE 5	Boötes V	Leo Minor I
IAU Name	⋯	J1921-6047	J1523+2723	J1500+0554	J1448+1728	J1415+3254	J1057+2852
Instrument	⋯	DECam	GMOS	GMOS	GMOS	GMOS	DECam
α_{2000}	deg	$290.396^{+0.003}_{-0.003}$	$230.775^{+0.001}_{-0.001}$	$225.059^{+0.001}_{-0.001}$	$222.104^{+0.002}_{-0.002}$	$213.909^{+0.001}_{-0.001}$	$164.261^{+0.005}_{-0.006}$
δ_{2000}	deg	$-60.784^{+0.001}_{-0.001}$	$27.395^{+0.001}_{-0.001}$	$5.909^{+0.001}_{-0.001}$	$17.468^{+0.001}_{-0.001}$	$32.914^{+0.001}_{-0.001}$	$28.875^{+0.004}_{-0.003}$
a_h	arcmin	⋯	$0.49^{+0.16}_{-0.12}$	⋯	$0.68^{+0.24}_{-0.17}$	$0.76^{+0.08}_{-0.07}$	⋯
$a_{1/2}$	pc	⋯	6^{+2}_{-2}	⋯	8^{+3}_{-2}	23^{+3}_{-3}	⋯
r_h	arcmin	$0.40^{+0.12}_{-0.08}$	$0.36^{+0.09}_{-0.07}$	$0.74^{+0.13}_{-0.11}$	$0.45^{+0.12}_{-0.09}$	$0.67^{+0.07}_{-0.06}$	$1.09^{+0.37}_{-0.35}$
$r_{1/2}$	pc	7^{+2}_{-2}	5^{+1}_{-1}	16^{+3}_{-3}	5^{+1}_{-1}	20^{+2}_{-2}	26^{+9}_{-9}
ϵ[a]	⋯	<0.4	$0.4^{+0.2}_{-0.2}$	<0.3	$0.6^{+0.1}_{-0.2}$	$0.2^{+0.1}_{-0.1}$	<0.4
P. A.	deg	87^{+30}_{-35}	152^{+14}_{-17}	131^{+44}_{-26}	77^{+10}_{-11}	18^{+13}_{-15}	74^{+49}_{-39}
$(m-M)_0$	mag	$18.73^{+0.09}_{-0.23}$	$18.28^{+0.19}_{-0.19}$	$19.30^{+0.22}_{-0.22}$	$17.97^{+0.17}_{-0.17}$	$20.04^{+0.15}_{-0.15}$	$19.56^{+0.11}_{-0.19}$
$D_\odot$	kpc	56^{+2}_{-6}	45^{+4}_{-4}	72^{+8}_{-7}	39^{+3}_{-3}	102^{+7}_{-7}	82^{+4}_{-7}
τ	Gyr	>11.7	13.5*	11.0*	10.0*	12.5*	>11.4
[Fe/H]	dex	< −1.4	−1.9*	−1.9*	−2.2*	−2.2*	< −1.9
M_V[b]	mag	$-1.3^{+0.4}_{-0.6}$	$-0.2^{+0.5}_{-0.8}$	$-1.6^{+0.4}_{-0.6}$	$0.4^{+0.4}_{-0.9}$	$-3.2^{+0.3}_{-0.3}$	$-2.4^{+0.4}_{-0.4}$
$\Sigma_{pi,\mathrm{ugali}}$[c]	⋯	25^{+5}_{-5}	⋯	⋯	⋯	⋯	22 ± 5
N_{GMOS}[c]	⋯	⋯	33^{+8}_{-7}	128^{+23}_{-20}	33^{+8}_{-7}	198^{+20}_{-19}	⋯
$E(B-V)$[d]	mag	0.054	0.042	0.039	0.030	0.013	0.018
$\mu_{\alpha*}$	mas yr^{-1}	$-0.33^{+0.31}_{-0.34}$	$+0.42^{+0.08}_{-0.09}$	⋯	$-1.82^{+0.13}_{-0.12}$	-0.22 ± 0.05	$-0.01^{+0.39}_{-0.40}$
μ_δ	mas yr^{-1}	$-0.80^{+0.35}_{-0.32}$	-0.75 ± 0.11	⋯	-0.93 ± 0.12	-0.28 ± 0.07	$-1.29^{+0.37}_{-0.40}$
$\Sigma_{ipi,\mathrm{MM}}$	⋯	⋯	2.0 ± 0.1	6.0 ± 0.0	⋯	2.8 ± 0.5	6.1 ± 0.1	2.9 ± 0.1

Notes. Age and metallicity were not constrained in our GMOS-N analyses; instead, we fixed these parameters to the values reported in this table, and indicate these quantities with an asterisk. For DELVE 3 and Leo Minor I, the age and metallicity posteriors were distributed against the allowed bounds (13.5 Gyr and [Fe/H] ∼ − 2.2); we therefore quote upper and lower limits on the age and metallicity (τ and [Fe/H]) at 84% confidence.
[a] The posterior distribution for the ellipticity of DELVE 3, Virgo II, and Leo Minor I peaked near $\epsilon = 0$, and we therefore quote an upper limit at 84% confidence. For these candidates, we do not quote a value of the elliptical half-light radius (a_h and $a_{1/2}$), and only quote the azimuthally averaged half-light radius (r_h and $r_{1/2}$).
[b] The uncertainty in the absolute magnitude, M_V, was calculated following Martin et al. (2008) and does not include the uncertainty on the distance.
[c] $\Sigma_{pi,\mathrm{ugali}}$ and N_{GMOS} refer to the modeled number of stars above the magnitude limit for our DECam and GMOS-N analyses, respectively.
[d] The $E(B-V)$ values listed here are calculated from the mean value of all DELVE DR2 sources within a 3′ radius around the centroid of each candidate.

luminosity of ultra-faint systems is contributed by the brightest stars, the absolute magnitude estimates have large uncertainties due to the stochastic sampling of the giant branch (Martin et al. 2008); however, they are reasonably robust to the assumed faint magnitude limit. This stochasticity drives much of the observed difference in the number of red giant branch stars candidate-to-candidate even for systems at similar absolute magnitudes. However, we also note that contaminating foreground/background interlopers passing our isochrone and astrometric cuts (e.g., stars from the Sagittarius stellar stream; see Section 6.1) may potentially induce some of the apparent variation in the observed number of red giant branch stars between candidates at roughly the same absolute magnitude.

4.2. DECam Data

For the candidates for which we obtained follow-up imaging with DECam (DELVE 1921-6047 and DELVE J1057+2852), we performed a maximum-likelihood fit to both the morphological and stellar population properties of each system using ugali. We modeled the structure of each candidate with a Plummer (1911) projected density profile, and we simultaneously fit a Bressan et al. (2012) isochrone to each candidate's observed g_0, r_0-band color–magnitude diagram. The eight free parameters for this fit to each candidate were the centroid R.A. and decl. (α_{2000} and δ_{2000}, respectively), semimajor axis length (a_h), ellipticity (ϵ), and position angle (P.A.) east-of-north of the Plummer profile, and the age (τ), metallicity (Z), and

distance modulus ($(m - M)_0$) of the synthetic isochrone. We sampled this parameter space using the affine-invariant MCMC ensemble sampler emcee (Foreman-Mackey et al. 2013), and we report the resulting parameter estimates with their corresponding uncertainties in Table 2.

Before each fit, we separated stars from background galaxies by applying the selection $0 \leqslant \mathrm{EXTENDED\_CLASS\_G} \leqslant 2$, which allowed for a high degree of stellar completeness at the cost of some galaxy contamination (see Drlica-Wagner et al. 2022). In lieu of artificial star tests for the DECam data, we opted to limit the structural fit to sources brighter than the local 10σ magnitude limit for each candidate, which we estimated within a 30′ radius around the discovery centroid of each system. The adopted magnitude limits are provided in Table 1.

4.3. Proper Motions from Gaia

We applied proper-motion mixture models to further confirm the reality of the systems and to measure the systemic proper motion of the six new satellites following Pace & Li (2019) and Pace et al. (2022). Briefly, we modeled the spatial and proper-motion distribution with a satellite and Milky Way foreground model. For the satellite distribution, we assumed a Plummer (1911) density profile for the spatial component and a multivariate Gaussian distribution for the proper-motion distribution. We adopted Gaussian priors for each candidate's extension, position angle, and ellipticity of each system using the ugali or GMOS-N modeling for the Plummer parameters.

We assumed that the Milky Way foreground was spatially constant over the small area examined and built the proper-motion distribution from the distribution of stars at much larger radii with the same target selection.

We utilized the excellent astrometry associated with Gaia DR3 (Gaia Collaboration et al. 2021; Lindegren et al. 2021), making the following selections to identify stars with good quality astrometry: RUWE < 1.4, astrometric_excess_noise_sig < 2, astrometric_params_solved > 3, and $|C^*| \leqslant 3\sigma_{C^*}(G)$. We removed foreground stars with a nonzero parallax ($\varpi - 3 \times \sigma_\varpi > 0$) and large proper motions. Specifically, we computed the tangential velocity of each star assuming it lies at the distance of the satellite and removed stars that have velocities significantly larger than the Milky Way escape velocity at that distance ($v_{\mathrm{tangential}} - 3 \times \sigma_{v_{\mathrm{tangential}}} < v_{\mathrm{escape}}$). We further applied a DECam g_0 versus $(g - r)_0$ color–magnitude filter based on an old, metal-poor ($\tau = 13.5$ Gyr, [Fe/H] ~ -2.2 dex) PARSEC isochrone, or a similar Gaia-based $G - G_{RP}$ color–magnitude filter to any stars that lacked g and r photometry in DELVE DR2. While this analysis could use color–magnitude information as a probabilistic component in the mixture model (e.g., McConnachie & Venn 2020; Battaglia et al. 2022), we have found that the use of accurate photometry does not require this inclusion to measure systemic proper motions (Pace et al. 2022). For a more detailed description of the methodology and data selections presented above, see Pace et al. (2022).

We were able to detect a proper-motion signal in five of the six candidates reported here, the single exception being DELVE J1500+0554 (see Section 5.2.1). Compared to many known dwarf galaxies with literature proper-motion measurements, the systems we present here have far fewer members in Gaia (e.g., Pace et al. 2022; Battaglia et al. 2022). This is primarily a consequence of the low luminosities of our candidates and not due to their distances. In Section 5, we review the properties of the stars that went into our measured proper motions for each candidate, and we provide these stars' Gaia DR3 source IDs in Appendix B, Table 3.

5. A Review of the Newly Discovered Systems

In the following subsections, we review the properties of each of the new candidate systems in greater detail. We begin by discussing the three candidates that we found to be compact before turning to the three candidates that we found to be more extended; we separate these candidates at $r_{1/2} = 15$ pc for convenience. Within this categorization scheme, we order the candidates by decreasing R.A., as in Tables 1 and 2. Figures 2–7 include the spatial distribution, radial profile, and color–magnitude diagram for stars in the vicinity of each candidate system.

5.1. Compact Candidates

5.1.1. DELVE J1921-6047 (DELVE 3)

Among the candidates presented in this work, DELVE J1921-6047 (Figure 2) represented the clearest and most significant detection at the time of discovery. It was identified in all four iterations of our simple search at significances of ∼ 6.8–9.5σ, and is clearly visible as a dense, circular association of blue stars in the color images available through the Legacy Surveys Sky Viewer as part of the Legacy Surveys DR10-early release. Our ugali fit to deeper DECam data revealed that DELVE J1921-6047 is a compact ($r_{1/2} = 7^{+2}_{-2}$ pc) and low-luminosity ($M_V = -1.3^{+0.4}_{-0.6}$ mag) stellar system consistent with an ancient,

metal-poor stellar population. The position of DELVE J1921-6047 in the size–luminosity plane of known Milky Way satellites (Figure 9) suggests that it is more consistent with the known population of ultra-faint star clusters than the population of known satellite galaxies. Following the convention that ultra-faint star clusters are named after the survey within which they were discovered, we name this system DELVE 3.

We tentatively detect a proper-motion signal for DELVE 3 based on two candidate member stars. There is also a nearby candidate blue horizontal branch star with a similar proper motion; however, it is too bright to pass our isochrone selection and therefore holds no weight in our proper-motion determination. This star was not identified as a probable member by the ugali analysis described in Section 4.2.

Although it is impossible to assess the origin of DELVE 3 in the absence of a spectroscopic radial-velocity measurement and/or metallicity measurement, the low photometric metallicity and large heliocentric distance ($D_\odot = 56^{+2}_{-6}$ kpc) suggested by the best-fit isochrone favor an accreted origin. Importantly, we observe that the system is relatively near to the (on-sky) positions of many ultra-faint dwarf galaxy systems believed to be associated with the Large and Small Magellanic Clouds (hereafter, the LMC and SMC, respectively). We further discuss this possible connection between DELVE 3 and the LMC/SMC in Section 6.3.

5.1.2. DELVE J1523+2723 (DELVE 4)

DELVE J1523+2723 (Figure 3) was detected with significances of 7.8σ and 8.1σ in the g, r searches run with the metal-poor and metal-rich isochrones, respectively. No i-band data is available in DELVE DR2 for this system, precluding its discovery in our g, i searches. The system is clearly visible in the Legacy Surveys Sky Viewer as a highly concentrated collection of ∼15 marginally resolved blue stars that appears comparable in angular size to an adjacent, unresolved spiral galaxy LEDA 1806653. Despite the clear spatial signature for this system at the image level, the DECam photometry was insufficient to constrain its properties or reveal a clear signature in color–magnitude space.

With the improved depth and resolution of our GMOS-N data, we were able to resolve many more stars in this system, revealing a clear main sequence in our color–magnitude diagram consistent with an ancient stellar population at a heliocentric distance of $D_\odot \sim 45^{+4}_{-4}$ kpc. The stellar population of DELVE J1523+2723 is adequately described by a PARSEC isochrone with [Fe/H] ~ -1.9 dex, but this measurement may be unreliable due to the dearth of red giant branch stars. Our structural fit to this system affirms that it is very compact ($r_{1/2} = 5^{+1}_{-1}$ pc) and faint ($M_V = -0.2^{+0.5}_{-0.8}$ mag). Based on these properties, we conclude that this system is most likely an ultra-faint star cluster, and we therefore name it DELVE 4.

We detect a proper-motion signal in DELVE 4 based on six faint candidate red giant branch stars. Although two of these stars are located at a fairly large distance relative to the center of the system ($\gtrsim 3r_h$), they have similar proper motions to the four stars near the system's centroid. The proper motion of DELVE 4 is discrepant with the Milky Way foreground proper motion in the region of sky near DELVE 4, and we conclude that we have confidently detected the systemic proper motion of DELVE 4. Speculatively, the large ellipticity ($\epsilon \sim 0.5$) and the presence of the two distant candidate members may suggest that DELVE 4 is undergoing tidal disruption. To confirm this scenario, radial-velocity measurements for the distant members are required.

DELVE J1921-6047 / DELVE 3 (DECam data)
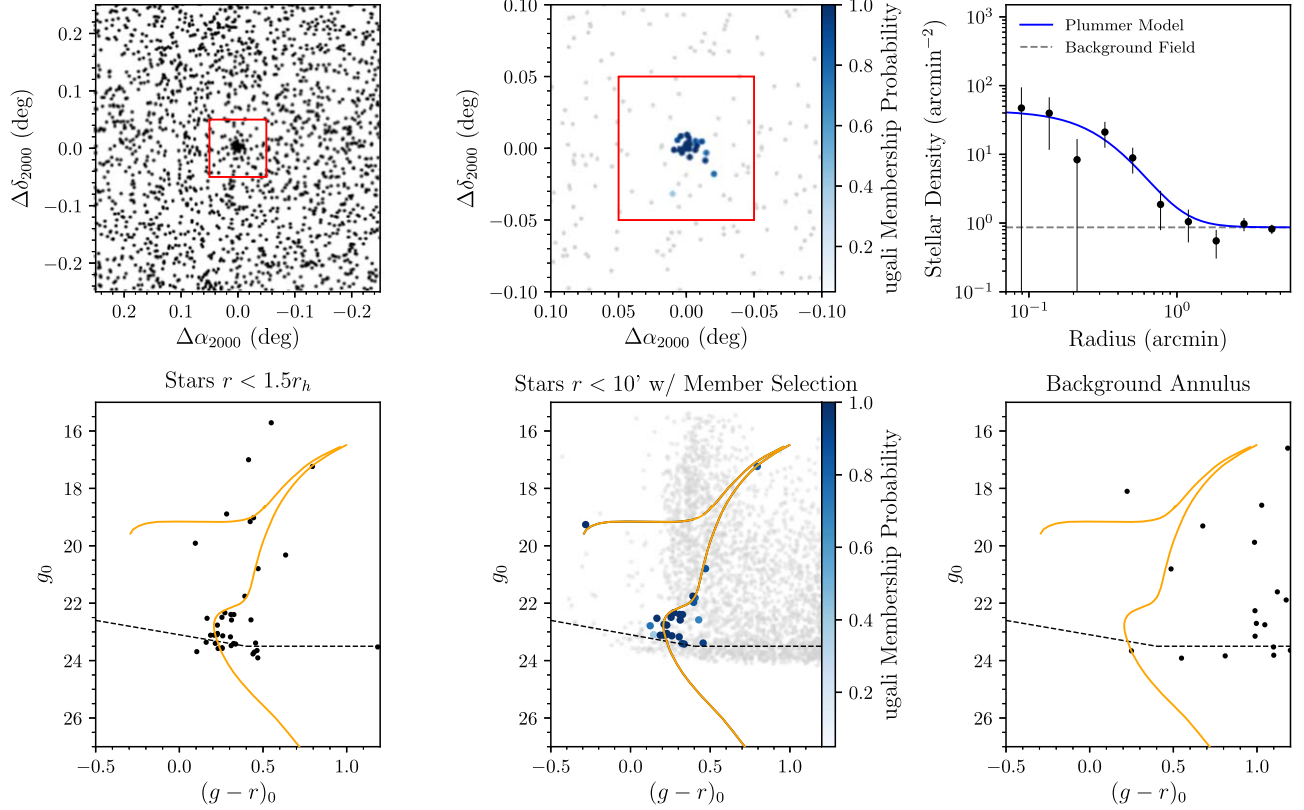
Figure 2. Diagnostic plots for DELVE J1921-6047 (DELVE 3) based on the DECam data. (Top left) Spatial distribution of all isochrone-filtered stars for a small region centered on the system. (Top center) A zoomed-in version of the top-left panel, now including only stars above the magnitude limit reported in Table 1. For ease of comparison, the red square denotes the same area as in the left panel. Stars with `ugali` membership probabilities >5% ($p_{ugali} > 0.05$) are shown in blue colors, whereas stars with ($p_{ugali} < 0.05$) are shown in gray. (Top right) Radial profile of isochrone-filtered stars centered on DELVE J1921-6047, again including only stars above the magnitude limit. The best-fit azimuthally averaged Plummer model is shown as a solid blue curve, and the background field density (as estimated within a concentric annulus with an inner radius of $10'$) is shown as a black dashed line. (Bottom left) Color–magnitude diagram of stars within a circular selection with a radius $1.5r_h$ for DELVE J1921-6047. A PARSEC isochrone with $\tau = 13.5$ Gyr, [Fe/H] $= -2.2$ dex is shown as a solid orange curve. The black dashed line denotes the magnitude limit used for our `ugali` analysis. (Bottom center) Color–magnitude diagram of stars within a radius of $r = 10'$, with stars identified as candidate members of DELVE J1921-6047 colored as in the top-center panel. (Bottom right) Color–magnitude diagram showing sources within the background annulus used to estimate the field density for the top-right panel. This annulus is equal in area to the circular selection used in the bottom-left panel.

5.1.3. DELVE J1448+1728 (DELVE 5)

We identified DELVE J1448+1728 (Figure 4) at $\sim 7.1\sigma$ in the g, r iterations of our `simple` search; again, no i-band data is available in DELVE DR2 for this system. Our initial diagnostic plots revealed two possible blue horizontal branch star candidates, and inspection of the color images in the Legacy Surveys Sky Viewer revealed a compact clustering of blue sources. However, the seemingly unusual distribution of these sources in the system was difficult to interpret. Furthermore, the Dark Energy Spectroscopic Instrument targeting overlay in the Sky Viewer incorrectly suggested that the bulk of sources in this system were either quasars or emission line galaxies (see Chaussidon et al. 2023 and Raichoor et al. 2023 for details on the target selection and expected contamination rates for each class of objects).

Despite these apparent anomalies, the GMOS-N data for DELVE J1448+1728 clearly reveals an extended main sequence consistent with an old, metal-poor stellar population. The distribution of isochrone-selected members in the GMOS-N FOV remains somewhat unusual, potentially suggesting that the system is either very diffuse and/or that contaminants may be obfuscating our view of the system. Our structural fit suggests that this system is exceedingly faint $M_V = +0.4^{+0.4}_{-0.9}$, with a

highly elliptical morphology ($\epsilon = 0.6^{+0.1}_{-0.2}$, $r_{1/2} = 5^{+1}_{-1}$ pc). One explanation for the sum total of these features is that the system is an ultra-faint star cluster that is undergoing tidal disruption, or simply evaporating due to N-body relaxation (e.g., Meylan & Heggie 1997). This would explain the apparently low luminosity (induced via mass loss) as well as the unusual spatial extension.

Ascertaining the true nature of DELVE J1448+1728 will likely require deep imaging over a wider field of view. Nonetheless, we observe a clear similarity between the properties of this system and those of the dissolving ultra-faint star cluster Kim 1. Specifically, Kim 1 features a similar lack of central concentration, moderately high ellipticity ($\epsilon = 0.4 \pm 0.1$), small size ($r_{1/2} = 5.2 \pm 0.6$ pc), and low luminosity ($M_V = 0.3 \pm 0.5$) (Kim & Jerjen 2015).[41] On the basis of this similarity, we presume that DELVE J1448+1728 is also an ultra-faint star cluster out of dynamical equilibrium, and we name the system DELVE 5.

---

[41] Both here and throughout the following subsections, we present comparisons to literature systems using the azimuthally averaged physical half-light radius, $r_{1/2}$. In cases where only the elliptical semimajor axis, $a_{1/2}$, is quoted in the literature, we derive a value for $r_{1/2}$ and its error via $r_{1/2} = a_{1/2}\sqrt{1-\epsilon}$. In doing so, we assume Gaussian errors for literature values of $r_{1/2}$ and ϵ.
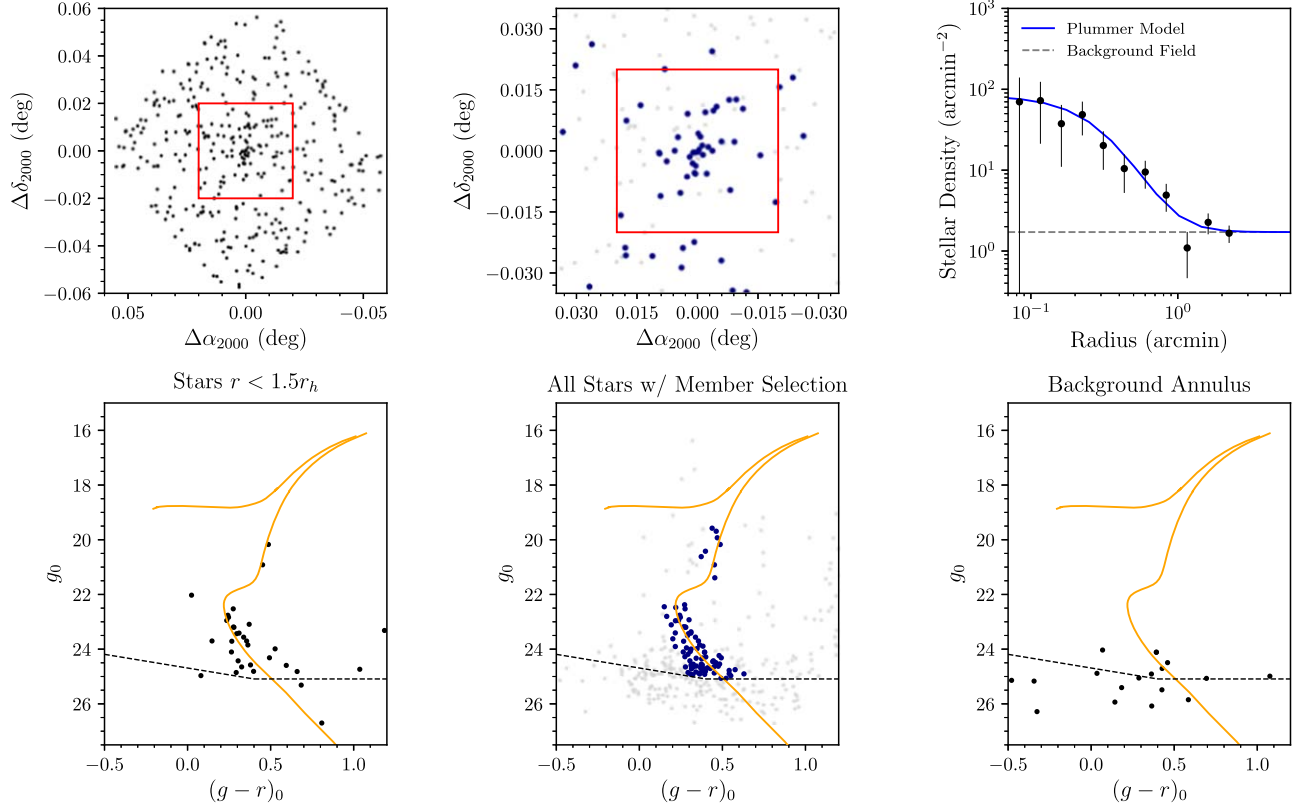
Figure 3. Diagnostic plots for DELVE J1523+2723 (DELVE 4), based on the GMOS-N data. (Top left) Spatial distribution of all stars in the full GMOS-N FOV; only our quality cut based on χ and *sharp* has been applied. (Top center) A zoomed-in version of the top left panel, now including only stars above the magnitude limit reported in Table 1. Stars with colors consistent with the isochrone to within 0.07 mag, accounting for photometric errors, are colored in blue and are presumed to be members. (Top right) Radial profile of isochrone-filtered stars centered on DELVE J1523+2723, again including only stars above the magnitude limit. The best-fit azimuthally averaged Plummer model is shown as a solid blue curve, and the background field surface density is depicted as a black dashed line. (Bottom left) Color–magnitude diagram of stars within a circular selection of $1.5 r_h$ centered on DELVE J1523+2723. The best-fit PARSEC isochrone is shown as a solid orange curve. The black dashed line denotes the magnitude limit used for our structural fit. (Bottom center) Color–magnitude diagram of stars within the GMOS-N FOV, with stars identified as candidate members colored as in the top-center panel. Stars identified as foreground based on their Gaia parallaxes and/or proper motions are excluded from this member selection, and are shown in gray. (Bottom right) Color–magnitude diagram for sources in a background annulus with inner radius of $\sim 2\overset{.}{'}4$. This annulus nearly traces the perimeter of the GMOS-N FOV, and is equal in area to the selection used in the bottom-left panel.

We detect a possible proper-motion signal for DELVE 5 based on three stars located at relatively large angular distances from the center of the system; these include two candidate blue horizontal branch stars and a red giant branch star at a similar magnitude. Oddly, we found no fainter members. It is possible that the signal we have identified is not the signal of DELVE 5, and it may instead represent the motion of another structure in the Milky Way halo. Radial velocities of these three stars would enable confirmation of our measurement, and would allow for a more detailed assessment of the system's dynamical state.

5.2. Extended Candidates

5.2.1. DELVE J1500+0554 (Virgo II)

DELVE J1500+0554 (Figure 5) was identified in all four iterations of our `simple` search with detection significances ranging from 5.6σ–7.9σ. It was visually confirmed in the Legacy Surveys Sky Viewer as a concentration of faint blue stars spread across a spatial region that was at least $1' \times 1'$ in size. This system is located in the constellation Virgo and falls $\sim 3°$ above the northern boundary of the Stripe 82 subsection covered by the second data release of HSC SSP (HSC SSP DR2); this explains why this candidate was not discovered in tandem with the Virgo I ultra-faint dwarf (Homma et al. 2016).

With our GMOS-N imaging, we confidently resolve stars three magnitudes below the main-sequence turnoff, revealing a large sample of possible member stars consistent with the best-fit old, metal-poor PARSEC isochrone. Our structural fit reveals that DELVE J1500+0554 is a relatively small, ultra-faint system ($r_{1/2} = 16^{+3}_{-3}$ pc; $M_V = -1.6^{+0.4}_{-0.6}$) at a distance of $D_\odot = 72^{+8}_{-7}$ kpc. This physical size places the system within the so-called "trough of uncertainty" (Conn et al. 2018a) in the $M_V - r_h$ plane within which the populations of ultra-faint star clusters and ultra-faint dwarf galaxies overlap (see Figure 9). Its closest analogs are Draco II, Cetus II, and Triangulum II, which have comparable half-light radii ($r_{1/2} = [16 \pm 4, \ 17 \pm 7, \ 17 \pm 4]$ pc, respectively) and luminosities $M_V = [-0.8^{+0.4}_{-1.0}, \ 0.0 \pm \ 0.7, \ -1.2 \pm \ 0.4]$ (Longeard et al. 2018; Drlica-Wagner et al. 2015; Carlin et al. 2017). All three of these known systems have proven difficult to classify. Neither Draco II nor Triangulum II have resolved velocity or metallicity dispersions, and thus have required more oblique arguments toward their classification. Toward this end, Baumgardt et al. (2022) searched for signatures of mass segregation in each of these systems. They found clear evidence for mass segregation in Draco II, and conclude that the system is a star cluster; by contrast, they find that Triangulum II is unsegregated, favoring a dwarf galaxy classification. Ji et al. (2019) also argued that Triangulum II

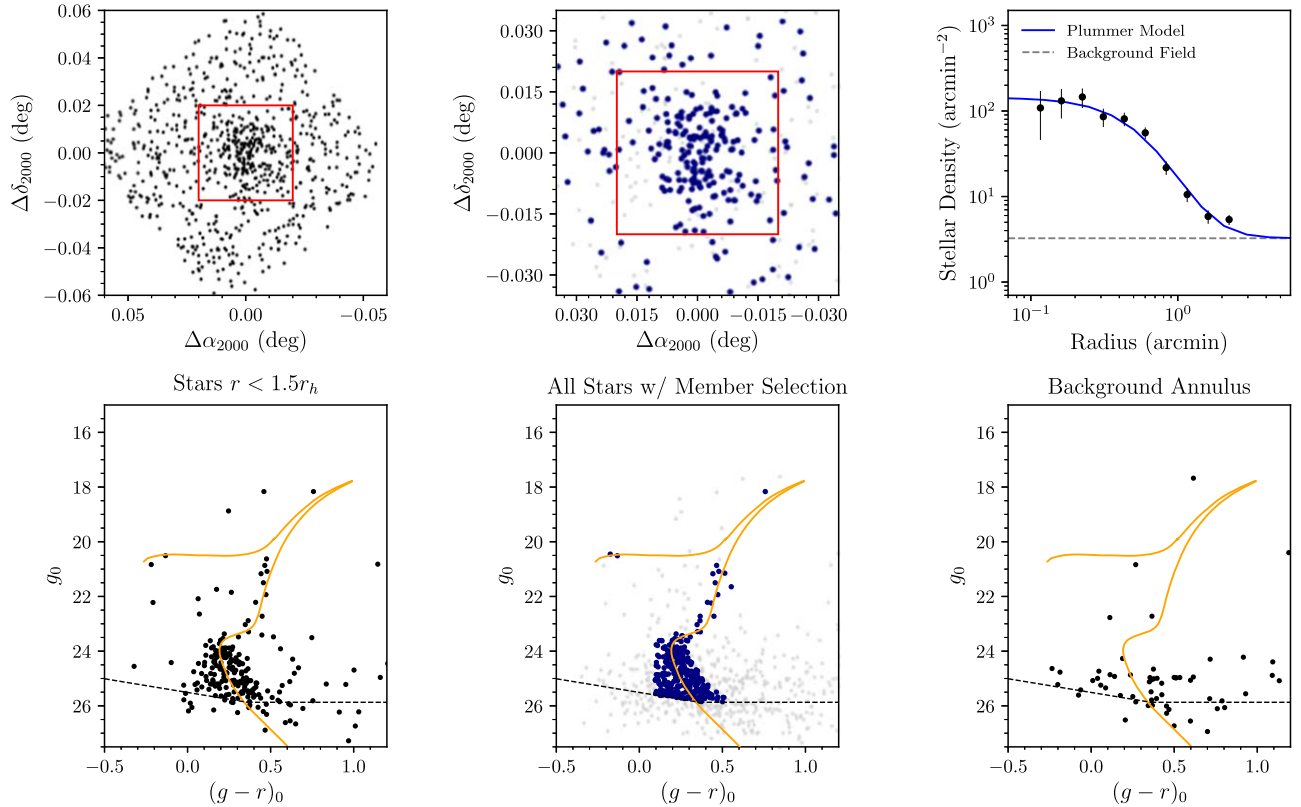## DELVE J1448+1728 / DELVE 5 (GMOS-N data)
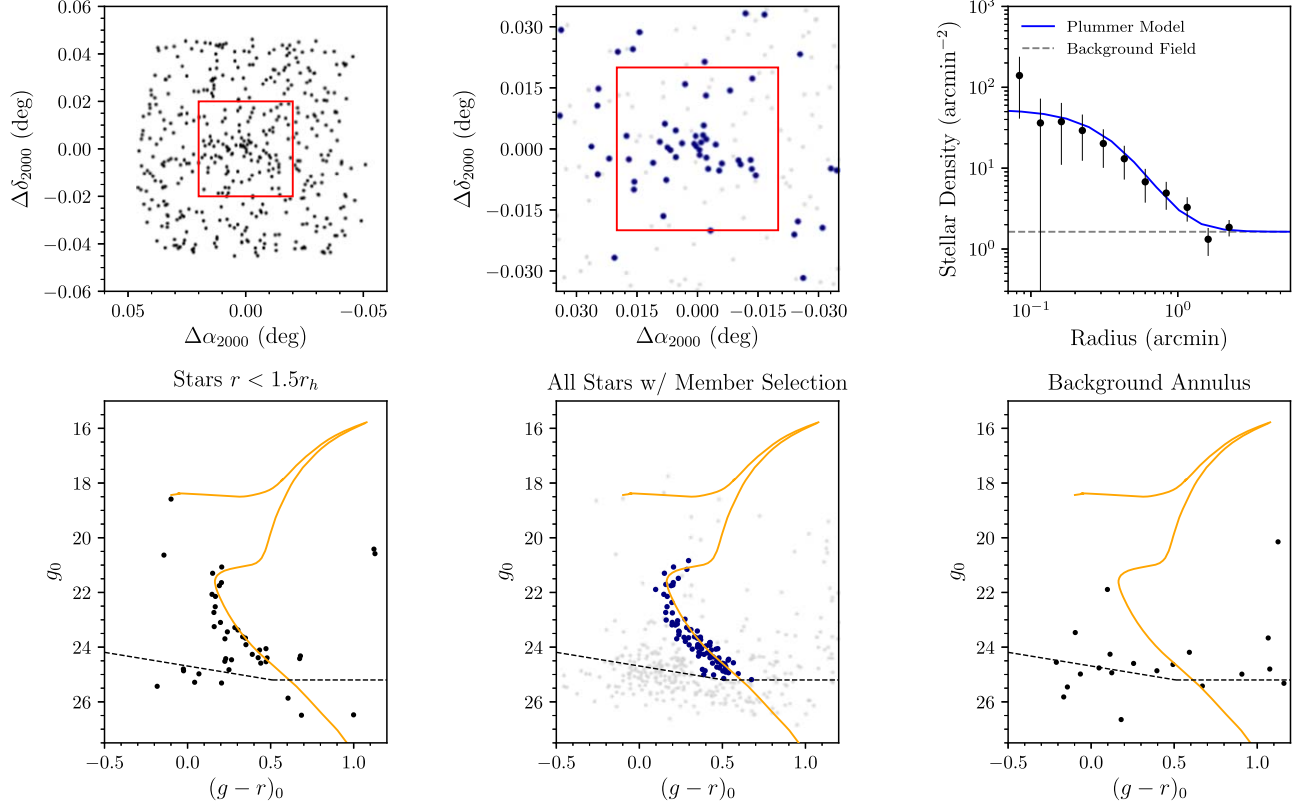
Figure 4. Diagnostic plots for DELVE J1448+1728 (DELVE 5) based on the GMOS-N data. Refer to Figure 3 for a detailed description of each panel. We highlight the unusual morphology of this system, which may suggest that it is not in dynamical equilibrium.

is a dwarf galaxy on the basis of its low neutron-capture element abundances measured through high-resolution spectroscopy. The reality of Cetus II has been questioned by Conn et al. (2018b), and we do not consider it further here.

As the above discussion reveals, the morphological properties of known ultra-faint stellar systems with $r_{1/2} \sim 16 - 17$ pc are insufficient to reach a firm determination about their classifications. Indeed, the cases of Draco II and Triangulum II convey that systems of this size could reasonably be either star clusters or dwarf galaxies in the absence of additional information. This effectively precludes us from making a high-confidence classification for DELVE J1500+0554. However, given the close similarity of *both* the absolute magnitude and half-light radius between DELVE J1500+0554 and Triangulum II, we believe that DELVE J1500+0554 is more likely to be an ultra-faint dwarf galaxy. We therefore adopt the name Virgo II, but emphasize that spectroscopic follow-up is necessary to reveal its true nature.

We do not detect a Gaia proper-motion signal for Virgo II. There are only two stars that pass the data quality and color–magnitude filtering within $4'$ of the Virgo II center. These two stars have discrepant proper motions. With radial-velocity information, it will likely be possible to distinguish which of these stars (if either) are members of the system and thereby constrain the proper motion. At this time, however, we do not report a proper-motion measurement for this system.

5.2.2. DELVE J1415+3254 (Boötes V)

DELVE J1415+3254 (Figure 6) was detected in both g, r iterations of the search, but only barely surpassed our 5.5σ detection threshold for the iteration that used a metal-rich

isochrone. Despite its low detection significance, we flagged this candidate for further investigation due to the apparent presence of three blue horizontal branch stars in our diagnostic plots from `simple`. We also identified that multiple stars in the immediate vicinity displayed self-consistent proper motions, supporting the reality of the system. With the deeper GMOS-N data, we were able to robustly constrain DELVE J1415+3254's properties, finding that it is an intermediate-size ($r_{1/2} = 20^{+2}_{-2}$ pc), relatively circular ($\epsilon = 0.2^{+0.1}_{-0.1}$), and low-luminosity ($M_V = -3.2^{+0.3}_{-0.3}$) system in the outer Milky Way halo ($D_\odot = 102^{+7}_{-7}$ kpc). Its stellar population is well described by the most metal-poor isochrone in our PARSEC grid ([Fe/H] = −2.2 dex).

Like Virgo II, DELVE J1415+3254's absolute magnitude and half-light radius place it in a region of parameter space where the populations of ultra-faint dwarf galaxies and ultra-faint star clusters overlap. This makes the system challenging to classify based on morphology alone. A physical size of 20 pc is not large enough to unambiguously suggest a dwarf galaxy classification for the system, especially given the measurement uncertainties at play. Ultra-faint systems with similar azimuthally averaged half-light radii and absolute magnitudes to DELVE J1500+0554 include Carina III, Willman 1, Tucana V, and Phoenix II, which have $r_{1/2} = [19 \pm 7, 20 \pm 2, 23 \pm 7, 28 \pm 5]$ pc and $M_V = [-2.4 \pm 0.2, -2.5 \pm 0.7, -1.1 \pm 0.6, -2.7 \pm 0.4]$, respectively (Torrealba et al. 2018; Muñoz et al. 2018; Simon et al. 2020; Mutlu-Pakdil et al. 2018). Li et al. (2018b) and Ji et al. (2020) both argued Carina III is a dwarf galaxy based on a large metallicity spread between member stars, and the latter work further supports this argument by establishing that the system displays low neutron-capture element abundances and no light element anticorrelations. Despite its irregular kinematic distribution, Willman et al.

DELVE J1500+0554 / Virgo II (GMOS-N data)
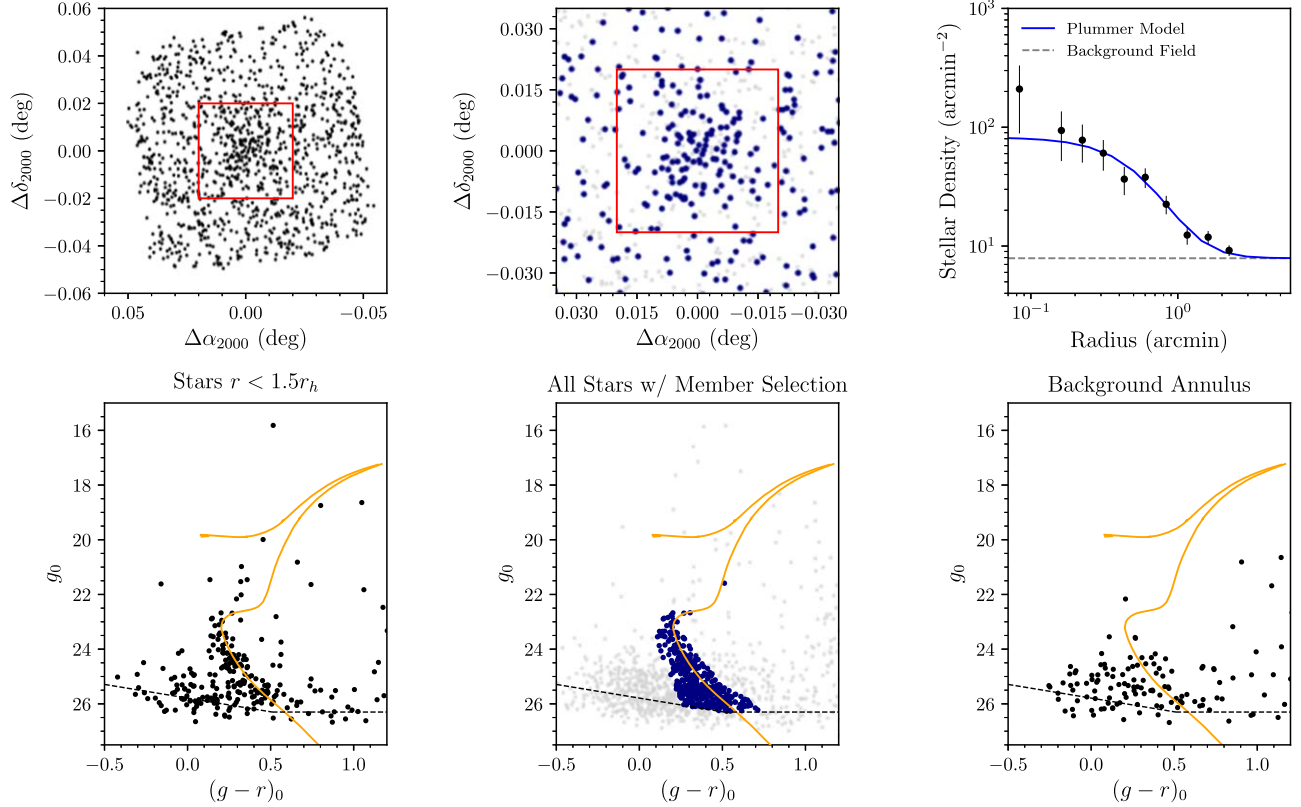
Figure 5. Diagnostic plots for DELVE J1500+0554 (Virgo II) based on the GMOS-N data. Refer to Figure 3 for a detailed description of each panel.

(2011) argued that Willman 1 is a dwarf galaxy on the basis of its metallicity spread. Simon et al. (2020) presented spectroscopy of Tucana V, but were unable to obtain limits on its velocity dispersion due to the small number of observed member stars. Lastly, Fritz et al. (2019) identified a large velocity dispersion for Phoenix II, robustly establishing its nature as a dwarf galaxy.

Based on the likelihood that three of the four systems with similar morphological properties to DELVE J1415+3254 are dwarf galaxies, we conclude that DELVE J1415+3254 is also most likely a dwarf galaxy. Accordingly, we name the system Boötes V following the convention that dwarf galaxy candidates are named after the constellation within which they reside; this name matches that given by the contemporaneous work by Smith et al. (2022).

Regardless of its classification, Boötes V features the most confident Gaia proper-motion signal of the six systems analyzed. It features a bright red giant branch star, two horizontal branch stars, and several fainter red giant branch stars with self-consistent proper motions, although the majority of our proper-motion measurement's precision is attributable to the brightest star alone.

Despite the absence of a radial-velocity measurement for Boötes V, we briefly explored its orbital properties using the `gala` package, assuming the package's default `MilkyWayPotential` Galactic potential (Price-Whelan 2017). We scanned through a range of heliocentric line-of-sight velocities for which the system is most likely bound to the Milky Way ($-300\,\mathrm{km\,s^{-1}} < v_{\mathrm{los}} < 600\,\mathrm{km\,s^{-1}}$) in steps of 5 km s^{-1}. At each velocity, we integrated the orbits for 10 Gyr and varied the distance and proper motion according to their observational errors. We found that Boötes V is on a polar orbit with a minimum predicted apocenter at a $v_{\mathrm{los}} \sim -80\,\mathrm{km\,s^{-1}}$. Interestingly, the system's proper motion implies a small pericenter

($r_{\mathrm{peri}} \lesssim 15-20$ kpc) across a wide range of possible radial velocities (see Figure 8). Such a close pericentric passage could result in tidal elongation or stripping of the system, as has been observed in a small number of known ultra-faint systems with small pericenters (e.g., Li et al. 2018a). Although we found no evidence for any morphological features suggestive of tidal disruption, this unique property of Boötes V strongly merits further study. Specifically, measurement of the system's radial velocity would allow confirmation of the low pericenter, and comparably deep imaging over a wider FOV would enable searches for distant member stars and extended structure around the system (e.g., Coleman et al. 2007; Sand et al. 2010, 2012; Mutlu-Pakdil et al. 2019, 2020).

5.2.3. DELVE J1057+2852 (Leo Minor I)

Like Boötes V, DELVE J1057+2852 (Figure 7) also lies near the northern edge of the sky accessible to DECam. It was detected in all four iterations of our search at significances of 6.1σ–7.3σ, despite the presence of CCD gaps in the surrounding field within DELVE DR2 (Figure 1). The system is visible in the Legacy Surveys Sky Viewer as a cloud of marginally resolved blue stars extending at least $2'$ in diameter (similar to Virgo II).

Despite our additional imaging of this system with DECam, the data available for DELVE J1057+2852 are relatively shallow for characterizing the structure of such a faint system at this distance ($D_\odot = 82^{+4}_{-7}$ kpc). In particular, the small sample of available member stars, combined with the lack of blue horizontal branch stars or a fully resolved main-sequence turnoff, resulted in considerable uncertainties on the best-fit distance and size of this system. These issues were likely compounded by the presence of stars from the Sagittarius stream in the foreground (see

DELVE J1415+3254 / Boötes V (GMOS-N data)

Figure 6. Diagnostic plots for DELVE J1415+3254 (Boötes V) based on the GMOS-N data. Refer to Figure 3 for a detailed description of each panel. We note that one candidate blue horizontal branch member star falls just outside our isochrone selection.

Section 6.1), as well as the existence of a moderately bright star positioned near the system centroid. In an attempt to better constrain its properties, we explored nearly two dozen different combinations of magnitude limits for the g, r bands, as well as different star/galaxy separation criteria. This resulted in a range of angular half-light radii of $r_h \sim 0.6' - 1.7'$, with shallower magnitude limits generally resulting in smaller angular sizes (and vice versa). The parameters we report come from our nominal choice to limit sources for the fit to stars above the 10σ magnitude limit, but we caution that deeper imaging is essential for accurate measurements for this candidate. Nonetheless, the large uncertainty on our measurement of r_h encompasses much of this range.

Accepting the caveats above, DELVE J1057+2852 is the most extended and second-most-luminous system we report in this work (after Boötes V), with an azimuthally averaged half-light radius of $r_{1/2} = 26^{+9}_{-9}$ pc and an absolute magnitude of $M_V = -2.4^{+0.5}_{-0.4}$ mag. At face value, the 1σ confidence interval for the half-light radius spans from systems like Draco II, Triangulum II, and Boötes V (on the small end) to systems like Horologium I, Sagittarius II, Horologium II, Boötes II, and Segue 2 (on the large end). Among the latter set of systems, Horologium I, Boötes II, and Segue 2 are accepted to be dwarf galaxies on the basis of their velocity and/or metallicity dispersions. Sagittarius II displays a small velocity dispersion but is most likely a star cluster (Longeard et al. 2020, 2021); however, this system is not closely analogous to DELVE J1057 +2852 due to its significantly brighter absolute magnitude ($M_V = -5.2 \pm 0.1$; Mutlu-Pakdil et al. 2018). Lastly, Horologium II lacks a sufficiently large spectroscopic sample to reach any firm conclusions about its classification (Fritz et al. 2019). Although the number of spectroscopically confirmed galaxies

at similar half-light radii is small, we believe that these comparisons generally support the conclusion that DELVE J1057+2852 is a dwarf galaxy. This is consistent with our earlier determinations that Virgo II and Boötes V, both of which are smaller in terms of half-light radius, are also likely dwarf galaxies. We therefore name the system Leo Minor I.

Lastly, we detected a proper-motion signal for Leo Minor I in Gaia through our mixture modeling approach; this signal is derived from three faint red giant branch stars. These three stars have similar radial velocities measured from the DEIMOS spectroscopy, and two of these stars have similar metallicities, giving us confidence in the accuracy of this proper-motion measurement despite the small sample size.

6. Potential Associations with Local Group Structures

We investigated whether the six stellar systems reported here may be associated with several Local Group structures, including the Sagittarius dwarf spheroidal galaxy, the Vast Polar Structure (VPOS), and the Magellanic Clouds. Although such associations remain largely speculative until radial-velocity measurements become available, we highlight these possible connections so as to inform follow-up observations and analyses.

6.1. The Sagittarius Dwarf Spheroidal

The Sagittarius dwarf spheroidal galaxy (Sgr), discovered by Ibata et al. (1994), represents one of the most significant stellar substructures in the Milky Way environment, featuring both a dense core positioned near the Galactic plane as well as an extended tidal stream stretching across the entire sky. In recent years, considerable effort has been invested into attempts to identify

DELVE J1057+2852 / Leo Minor I (DECam data)
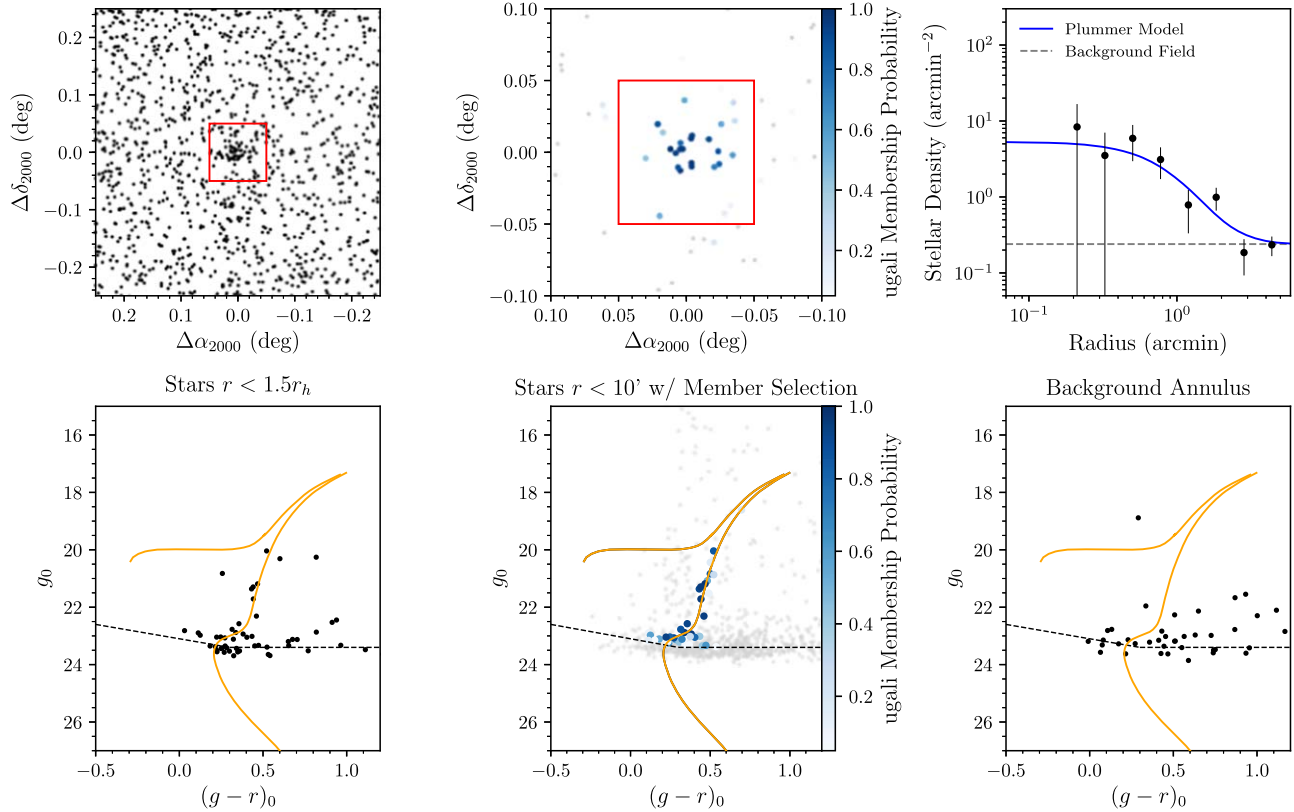
Figure 7. Diagnostic plots for DELVE J1057+2852 (Leo Minor I) based on the DECam data. Refer to Figure 2 for a detailed description of each panel. Although the total number of stars above the magnitude limit is relatively small, the radial stellar density profile appears accurately represented by the best-fit Plummer model.

stellar systems that may have accreted along with Sgr, including both globular clusters and dwarf galaxies (e.g., Da Costa & Armandroff 1995; Bellazzini et al. 2003; Forbes & Bridges 2010; Law & Majewski 2010a; Luque et al. 2017; Garro et al. 2021).

Two of our dwarf galaxy candidates, Leo Minor I and Virgo II, lie at low latitudes relative to the Sgr stream (Sgr stream latitude of $|\beta| < 11°$, in the coordinate system of Law & Majewski 2010b), raising the possibility of a similar association for these systems. To investigate whether these candidates could plausibly have been accreted with Sgr, we turned to the Sgr models of Vasiliev et al. (2021), who performed tailored N-body simulations of the orbit of Sgr around the Milky Way in the presence of the LMC. We selected all simulated star particles within a radius of 5° centered on Leo Minor I and Virgo II, and considered whether the distances and velocities of the particles matched those of the two candidates, where possible.

Near Leo Minor I, we found two groups of Sgr stars: one group with heliocentric distances $D_\odot \sim 10 - 30$ kpc and line-of-sight velocities -165 km s^{-1} to -20 km s^{-1}, and another group with $D_\odot \sim 45 - 75$ kpc and $v_{los} \sim 160$ km s^{-1} to -200 km s^{-1}. Leo Minor I is consistent with membership in the latter group on the basis of its heliocentric distance ($D_\odot = 82^{+4}_{-7}$ kpc), although radial-velocity information will be required to confirm or dispute this possible association. At the location of Virgo II, we observe three separate groups/wraps of Sgr stars in the $D_\odot - v_{los}$ plane. The farthest of these groups lies at $D_\odot \sim 45 - 60$ kpc, to be compared with $D_\odot = 72^{+8}_{-7}$ kpc for the candidate dwarf. This difference in distance weakly disfavors an association between Virgo II and Sgr, although a proper-motion and/or radial-velocity measurement for the former would allow for a more informative comparison.
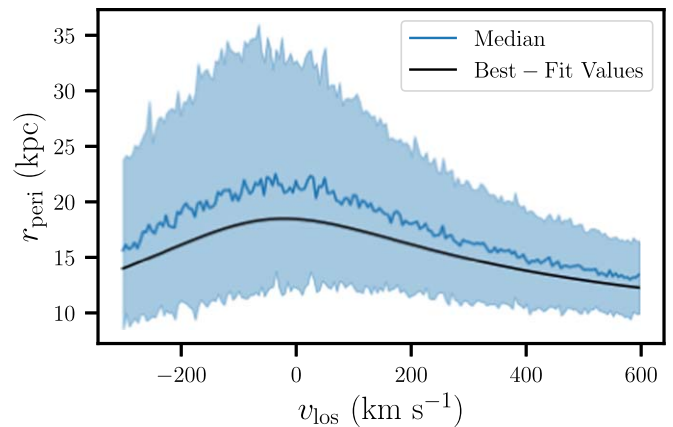
Figure 8. Predicted orbital pericenter (r_{peri}) across a range of possible line-of-sight velocities (v_{los}) for Boötes V. The black line uses the median values for the proper motion and distance, whereas the blue line and bands are from MCMC sampling of the proper motion and distance errors.

6.2. The Vast Polar Structure

We considered whether any of the dwarf galaxy candidates presented here are plausibly associated with the VPOS of the Milky Way (Pawlowski et al. 2012). A substantial fraction of the observed Milky Way satellite galaxies have aligned orbital planes oriented nearly perpendicular to the Milky Way's stellar disk (Pawlowski & Kroupa 2013, 2020), extending to the faintest galaxies (Fritz et al. 2018) with updated Gaia EDR3 proper motions (Li et al. 2021).
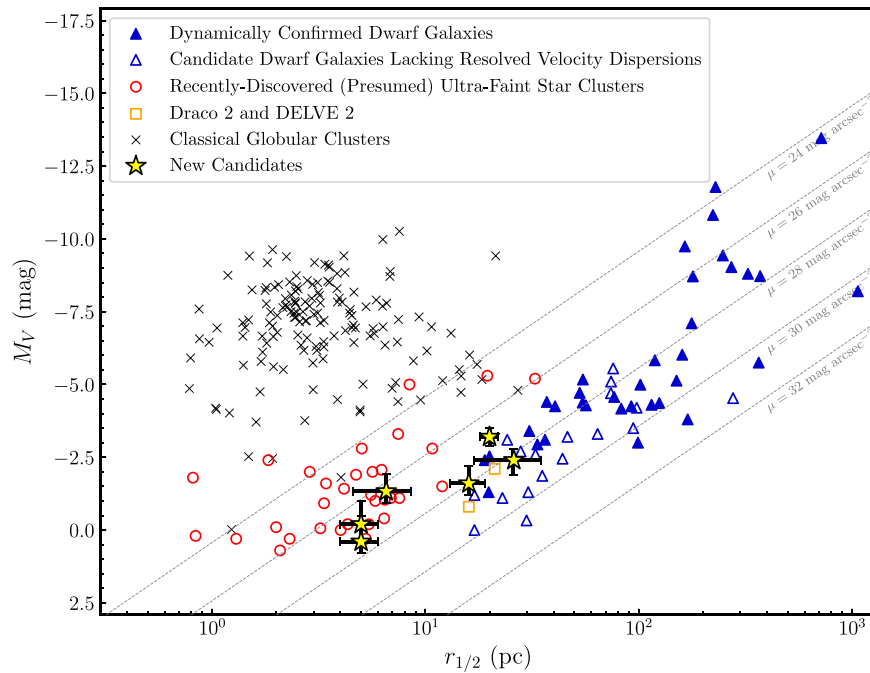
Figure 9. Absolute V-band magnitude (M_V) vs. azimuthally averaged physical half-light radius ($r_{1/2}$) for various different populations of Milky Way satellites. Dynamically confirmed dwarf galaxies (i.e., those with resolved velocity dispersions) are shown as solid blue triangles, and candidate dwarf galaxies (with unresolved dispersions) are shown as open blue triangles. "Classical" Milky Way globular clusters from Harris (1996), 2010 edition, are shown as black crosses. Recently discovered systems presumed to be ultra-faint star clusters are shown as open red circles. The systems DELVE 2 (Cerny et al. 2021a) and Draco II (Laevens et al. 2015), which have as-yet unknown classifications, are included as orange squares. For a complete reference list, see Appendix A of Cerny et al. (2023). Lastly, the six new candidates presented in this work are shown as yellow stars. From left to right (i.e., in order of increasing $r_{1/2}$), these are DELVE 4 and DELVE 5 (at the same $r_{1/2}$, where DELVE 4 is brighter), DELVE 3, Virgo II, Boötes V, and Leo Minor I.

Specifically, we considered two quantities to assess VPOS membership: the minimum possible angle, $\theta_{\rm pred}$, between the VPOS normal and the satellite's orbital pole based on spatial information alone (Pawlowski & Kroupa 2013), and the probability, $p_{\rm VPOS}$, that the satellite's orbital pole lies within some angular tolerance, $\theta_{\rm in,VPOS}$, of the VPOS normal after incorporating proper motions and measurement uncertainties. Since all but one of our candidates do not have measured line-of-sight velocities, we calculated $p_{\rm VPOS}$ for a range of assumed velocities from -600 km s$^{-1} < v_{\rm los} < +600$ km s^{-1} (see Figure 10). We adopt the same methodology and VPOS parameters as in prior work (Fritz et al. 2018; Li et al. 2021), namely the assumed VPOS normal ($l_{\rm MW}$, $b_{\rm MW}$) = (169°.3, −2°.8) and angular tolerance $\theta_{\rm in,VPOS} = 36°.87$, corresponding to circles that encompass 10% of the sky.

We display the results of this analysis in Figure 10. In brief, we found that the spatial positions and proper-motion measurements favor membership for Boötes V ($0.5 < p_{\rm VPOS} < 0.8$), but disfavor membership for Leo Minor I ($p_{\rm VPOS} \lesssim 0.4$ across all radial velocities). We could not explore the same possibility for Virgo II given the lack of proper-motion or radial-velocity measurement. However, we do observe that its spatial position suggests a minimum angle $\theta_{\rm pred} \sim 33°$. This is less than the tolerance adopted by Fritz et al. (2018) and Li et al. (2021), suggesting that an association may be possible.

Although the orbits of globular clusters and stellar streams do not preferentially align with the VPOS (Riley & Strigari 2020), we also explored the possibility VPOS membership for our ultra-faint star cluster candidates (DELVE 3–5) in the same manner. We found that DELVE 3's membership is ruled out based on its spatial position alone, while DELVE 4 and DELVE 5 are favored or heavily favored

to be VPOS members ($0.5 < p_{\rm VPOS} < 1$), although the degree depends on the radial velocity.

6.3. The Magellanic Clouds

A growing body of observational evidence suggests that many of the known Milky Way satellite galaxies were accreted along with the Magellanic Clouds as they fell into the Milky Way (e.g., Bechtol et al. 2015; Koposov et al. 2015; Sales et al. 2017; Kallivayalil et al. 2018; Patel et al. 2020; Fritz et al. 2019; Erkal & Belokurov 2020). Although five of our six candidates are unlikely to be associated with the LMC/SMC on the basis of their spatial positions, we do observe that DELVE 3 lies in the broad region of sky within which satellites of the Magellanic Clouds have been discovered (Bechtol et al. 2015; Koposov et al. 2015). It is therefore worthwhile to consider whether DELVE 3 may also be an accreted satellite associated with the Magellanic Clouds.

At present, DELVE 3 is located at a (3D) separation of 43 kpc from the LMC and 32 kpc from the SMC, compared to its 49.5 kpc separation from the Galactic Center. Comparing the on-sky position and distance of DELVE 3 to the numerical simulations of Jethwa et al. (2016), we found that the system resides at a position where the expected density of LMC satellite debris is much lower than many of the DES LMC satellite candidates. However, the system's Galactocentric distance falls within the range where it is plausible for a connection between the systems to exist. Plotting the solar-reflex-corrected proper-motion vector for DELVE 3, we also observed that DELVE 3 is moving in the same broad direction as multiple dwarf galaxies believed to be associated with the LMC/SMC (Kallivayalil et al. 2018; Patel et al. 2020). Thus, we see no reason to rule out a possible association between DELVE 3 and the Magellanic Clouds at this time, but we emphasize that spectroscopy
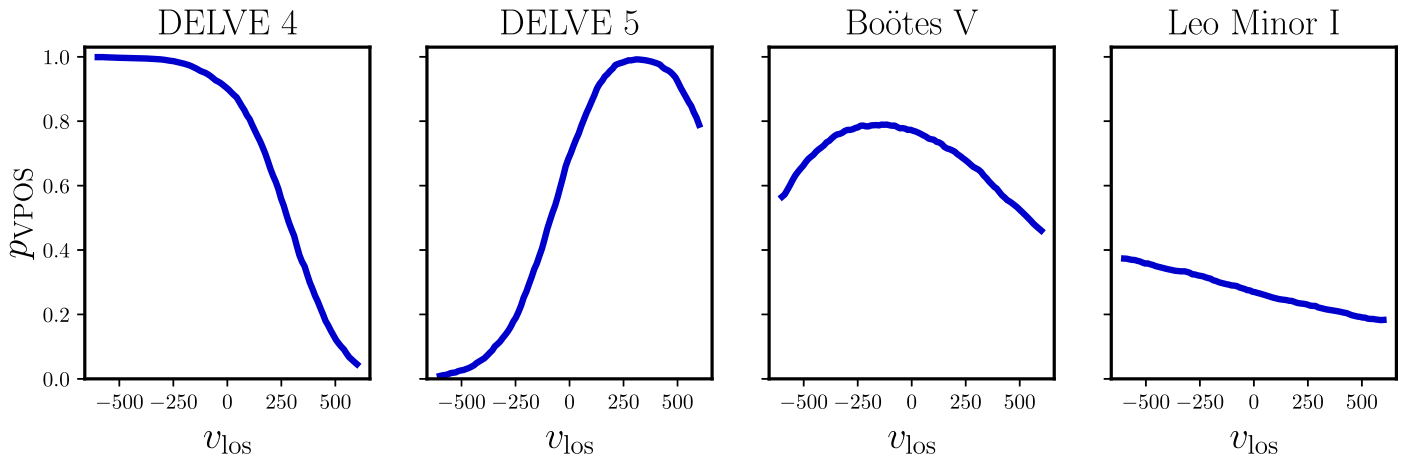
Figure 10. Predicted VPOS membership probability $p_{\rm VPOS}$ as a function of radial velocity for the five candidates lying at $\theta_{\rm pred} < 36°9$. We exclude DELVE 3 because its spatial position falls well outside the VPOS plane, and we exclude Virgo II because we were unable to measure its proper motion. Overall, we find that DELVE 4, DELVE 5, and Boötes V are promising VPOS member candidates, and that VPOS membership for Leo Minor I is disfavored but not ruled out. We caution that not all radial velocities are equally probable, and that radial velocities at the extremes of the ranges presented here may correspond to orbits that are unbound.

(and a higher-confidence proper-motion measurement) will be required to confirm or dispute a connection.

7. Summary

We have presented the discovery of six ultra-faint stellar systems, all detected in the second data release of the DECam Local Volume Exploration survey. To better characterize the properties of these systems, we obtained deeper imaging of all six systems with either DECam or GMOS-N. For the four candidates with GMOS-N imaging, the excellent depth and image quality of the observations allowed us to probe stars several magnitudes deeper than the main-sequence turnoff. While the DECam imaging for the remaining two candidates represented only a minor improvement over the discovery data, we were nonetheless able to characterize the candidates' structure. Based on maximum-likelihood fits, we determined that three of the six systems are more spatially extended ($r_{1/2} > 15$ pc), while the other three systems are more compact ($r_{1/2} < 10$ pc). We measured the proper motions of five of these six candidates, although two of these measurements are tentative due to uncertainty in the membership of the stars from which they were derived. The morphological, stellar population, and proper-motion properties of each candidate are summarized in Table 2.

The three compact systems, which we named DELVE 3, DELVE 4, and DELVE 5, likely represent ultra-faint star clusters. These systems all feature an old, metal-poor stellar population, favoring an accreted origin for each. Toward this end, we argued that DELVE 3 may represent a distant satellite of the Magellanic Clouds, and that DELVE 4 and DELVE 5 may be members of the Milky Way satellite plane known as the VPOS. Radial velocities will be needed to test these possibilities.

The three remaining candidates, which we named Virgo II, Boötes V, and Leo Minor I, most likely represent ultra-faint dwarf galaxies on the basis of their sizes and luminosities. However, we could not rule out a star cluster nature for these systems, and spectroscopic velocity and/or metallicity dispersion measurements will be necessary to assess their nature. We explored whether Leo Minor I and Virgo II may be associated with the Sagittarius dwarf spheroidal, and found that the latter may possibly be associated. We also found that Boötes V is a promising VPOS member candidate, potentially adding to the roster of systems associated with this planar structure.

Our results offer a preview of the ultra-faint satellite systems soon to be discovered by the Vera C. Rubin Observatory and its Legacy Survey of Space and Time (LSST; Ivezić et al. 2019). In particular, it is expected that a significant majority of the Milky Way satellite galaxies and star clusters that the Rubin LSST will soon discover will lie at luminosities similar to the candidates presented here ($M_V \gtrsim -3.2$ mag; see, e.g., Hargis et al. 2014; Ivezić et al. 2019; Nadler et al. 2019; Manwadkar & Kravtsov 2022). Although candidates in this luminosity range have repeatedly been discovered since SDSS, the Rubin LSST will dramatically increase the volume within which we can detect these systems. As is already apparent, the physical classification of these faint systems will be one of the major challenges in the era of Rubin.

Appendix A
Completeness Curves for the GMOS-N Photometry

In Figure 11, we depict the completeness of our GMOS-N photometry as a function of magnitude, derived from the artificial star tests described in Section 3.1.
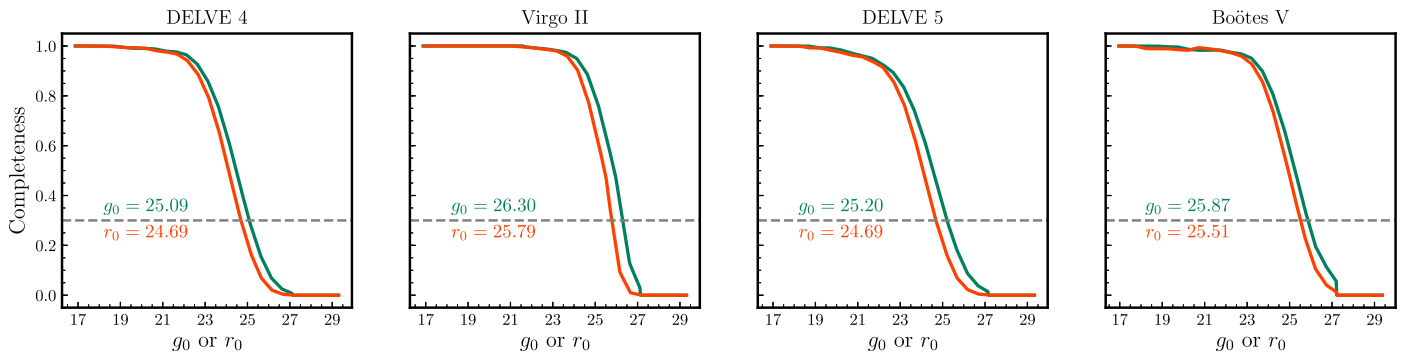

Figure 11. Completeness as a function of extinction-corrected magnitude (g_0 or r_0) for the four candidates with GMOS-N imaging, after application of the χ and *sharp* cuts described in the main text. The g-band completeness curve is shown in green, while the r-band completeness curve is shown in red. The 30% completeness limit for both bands is denoted by a gray dashed line, with the corresponding magnitude limits labeled above and below; these match the values given in Table 1.

---

42 https://github.com/esheldon/fitsio
43 http://healpix.sourceforge.net
44 https://github.com/healpy/healpy
45 https://github.com/DarkEnergySurvey/ugali

Appendix B
Candidate Members Stars Identified Based on Gaia Proper Motions

In Table 3, we list the member stars in each candidate that have proper motions measured by Gaia. We report only stars with mixture model probabilities $p_{MM} > 0.01$ (see Section 4.3 for details). The one exception to this probability cut is Virgo II, for which we report the two stars that may individually be members but that have discrepant proper motions (see Section 5.2.1).

Table 3
Candidate Proper-motion Members for Each Host Reported in This Work

Host	Source ID	R.A. (deg)	Decl. (deg)	p_{MM}
Virgo II	1159816202723001344	225.055304	5.909133	0.0
Virgo II	1159816404586450304	225.044828	5.916107	0.0
Boötes V	1478121378694742912*	213.909901	32.906644	1.00
Boötes V	1478121382994560256*	213.911812	32.914049	1.00
Boötes V	1478121413054482560	213.921037	32.922418	1.00
Boötes V	1478121584853173888	213.907406	32.912497	1.00
Boötes V	1478121584853174272*	213.902565	32.919849	1.00
Boötes V	1478121722292128768*	213.930665	32.939983	0.99
Boötes V	1478126743113866624	214.002746	32.945834	0.04
Boötes V	1478127773905897344	213.974961	32.982115	0.06
Leo Minor I	731478564536994432	164.272010	28.854826	0.99
Leo Minor I	731478663321185152	164.274357	28.876532	0.98
Leo Minor I	732979913304939776	164.285114	28.893772	0.96
DELVE 3	6445895198535725568	290.409730	−60.779749	0.98
DELVE 3	6445895232895460096	290.374884	−60.784377	0.99
DELVE 3	6445895645212360192	290.407766	−60.747341	0.05
DELVE 4	1270955387816956928*	230.761381	27.359978	1.00
DELVE 4	1270955387817087232*	230.768366	27.367744	0.99
DELVE 4	1270955800133818240*	230.779884	27.384258	1.00
DELVE 4	1270956006292249984	230.774651	27.394922	1.00
DELVE 4	1270956006292370176	230.785858	27.394184	1.00
DELVE 4	1270956006292379648*	230.773749	27.395964	1.00
DELVE 5	1236269365075548672	222.081767	17.409420	0.79
DELVE 5	1236270945623558912	222.094775	17.473537	1.00
DELVE 5	1236271564098855296	222.178859	17.481047	0.03
DELVE 5	1236317949745662336	222.075186	17.496322	0.92

Note. Stars with an asterisk refer to those that overlap with the candidate member stars identified by the Gaia-based wavelet transform search algorithm from Darragh-Ford et al. (2021).

Appendix C
Testing the Robustness of the GMOS-N Structural Fits

C.1. Injection-recovery Tests with Simulated Stellar Systems

To validate the performance of our binned Poisson maximum-likelihood structural fit of the GMOS-N data, we performed a suite of simulation-injection-recovery tests. We generated simulated satellites over a range of parameters that span our observed candidates (Table 4). For each choice of input parameters, we simulated the satellite and foreground stellar distribution by drawing a Poisson random sample of stars from our model with the detection fraction mask applied. We fit the simulated stellar distribution using the same procedure that we applied to the GMOS-N data, characterizing each parameter's posterior probability distribution with the affine-invariant ensemble sampler, emcee. We estimated the best-fit parameters and their uncertainties by calculating the median, 16th percentile (p_{16}), and the 84th percentile (p_{84}) of the posterior probability distribution. To assess the ability of our algorithm to recover the input parameter values within the derived uncertainties, we calculated the pull distribution, $\mathcal{P}$, for each parameter using the asymmetric definition from Demortier & Lyons (2002),

$$\mathcal{P}(\theta) = \begin{cases} \frac{(\theta - \theta_0)}{\theta_{\mathrm{UL}} - \theta}, & \text{if } \theta \leqslant \theta_0. \\ \frac{(\theta - \theta_0)}{\theta_{\mathrm{LL}} - \theta}, & \text{otherwise,} \end{cases} \quad \text{(C1)}$$

where θ is the best-fit value of the parameter (i.e., the median of the posterior), θ_{UL} and θ_{LL} are, respectively, the upper and lower limit on the best-fit value (i.e., estimated from the minimum interval containing the peak and 68% of the posterior), and θ_0 is the input value of the parameter. In the case that our procedure accurately captures the statistical scatter in the fit parameter and its uncertainty, the pull distribution will be described by a unit normal distribution, $\mathcal{P}(\theta) \sim \mathcal{N}(0, 1)$. The pull distributions for the set of input parameters over our full suite of simulations can be seen in Figure 12. To explore the dependence of our fits on the input parameter values, we also examined the mean and standard deviation of the pull distribution binned by input parameters.

We find that the pull distribution is well described by $\mathcal{N}(0, 1)$ over the sampled parameter space. However, there are several regions where our peak/interval summary statistics are inadequate to describe the posterior distribution. This generally occurs when the posterior runs up against bounds on the

Table 4
Range of Simulated Parameters

Parameter	Range	Unit
Observed Stars (Richness)	[25, 250]	
Centroid Coordinate (x)	[1100, 2200]	pixels
Centroid Coordinate (y)	[500, 1750]	pixels
Extension (a_h)	[50, 600]	pixels
Ellipticity (ϵ)	[0, 0.8]	
Position Angle (P.A.)	[0, 180]	deg
Surface Density (Σ)	[1, 50]	stars/Mpix

allowed ranges that parameters can take. We describe specific cases below.

1. At small values of ellipticity, the posterior is bounded by the prior of $\epsilon \geqslant 0$. In these cases, the posterior is one-sided, peaking at $\epsilon = 0$. Our peak/interval summary statistics are insufficient to describe the posterior distribution, and our pull distribution will be biased. This is not particularly concerning because for real systems in this regime, we instead quote an upper limit on ϵ derived from the 84th percentile of the posterior distribution.

2. In cases where the $\epsilon \sim 0$, the position angle is poorly constrained. However, because the position angle is bounded to values $0 < \mathrm{P.A.} < 180°$, there will be a maximum separation between the fit and true values, as well as a maximum size of the 68% interval. Due to these bounds, the pull distribution is not well summarized by a unit normal distribution.

3. The richness is restricted to positive values. In cases where the true richness is low (richness ~ 25) and the extension is large (extension > 400 pix), the posterior probability distribution for the richness will sometimes run up against the bound at richness = 0. Similar to the previous two cases, these situations would be identified in real systems when the posterior was inspected. In these cases, it is likely that the system would have been rejected from the sample.

Each of these situations would be identified during inspection of the candidate fit results, and a different technique would be applied to summarize the posterior probability distribution (e.g., deriving a 84% confidence level upper limit). Regardless, these cases are included in the simulations shown in Figure 12, and it can be seen that they have a relatively small impact in overall performance of the algorithm.
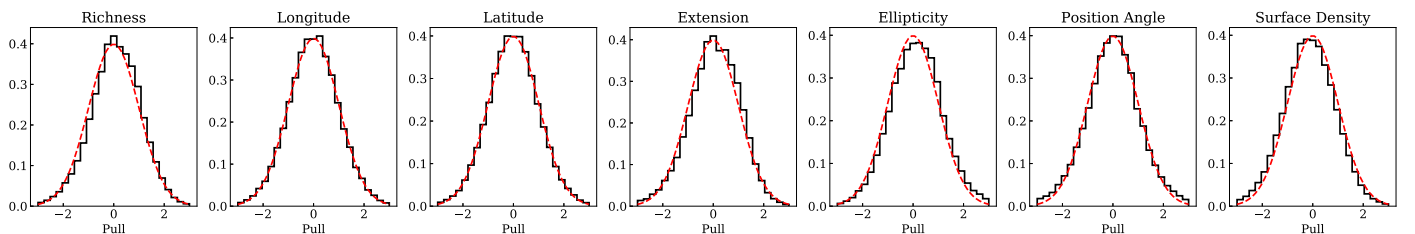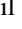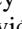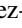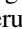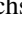

Figure 12. Pull distribution for each structural parameter in the binned Poisson maximum-likelihood fit of the GMOS-N data. The pull is calculated as the difference between the fit value of the parameter and the input parameter divided by the fit uncertainty. The black histogram shows the pull distribution derived from $\sim 45{,}000$ simulations, while the red dashed line shows a standard unit normal distribution, $\mathcal{N}(0, 1)$.

ORCID iDs

W. Cerny ⓘ https://orcid.org/0000-0003-1697-7062
C. E. Martínez-Vázquez ⓘ https://orcid.org/0000-0002-9144-7726
A. Drlica-Wagner ⓘ https://orcid.org/0000-0001-8251-933X
A. B. Pace ⓘ https://orcid.org/0000-0002-6021-8760
B. Mutlu-Pakdil ⓘ https://orcid.org/0000-0001-9649-4815
T. S. Li ⓘ https://orcid.org/0000-0002-9110-6163
A. H. Riley ⓘ https://orcid.org/0000-0001-5805-5766
D. Crnojević ⓘ https://orcid.org/0000-0002-1763-4128
C. R. Bom ⓘ https://orcid.org/0000-0003-4383-2969
J. A. Carballo-Bello ⓘ https://orcid.org/0000-0002-3690-105X
J. L. Carlin ⓘ https://orcid.org/0000-0002-3936-9628
A. Chiti ⓘ https://orcid.org/0000-0002-7155-679X
Y. Choi ⓘ https://orcid.org/0000-0003-1680-1884
M. L. M. Collins ⓘ https://orcid.org/0000-0002-1693-3265
E Darragh-Ford ⓘ https://orcid.org/0000-0002-8800-5652
P. S. Ferguson ⓘ https://orcid.org/0000-0001-6957-1627
M. Geha ⓘ https://orcid.org/0000-0002-7007-9725
D. Martínez-Delgado ⓘ https://orcid.org/0000-0003-3835-2231
P. Massana ⓘ https://orcid.org/0000-0002-8093-7471
S. Mau ⓘ https://orcid.org/0000-0003-3519-4004
G. E. Medina ⓘ https://orcid.org/0000-0003-0105-9576
R. R. Muñoz ⓘ https://orcid.org/0000-0002-0810-5558
E. O. Nadler ⓘ https://orcid.org/0000-0002-1182-3825
N. E. D. Noël ⓘ https://orcid.org/0000-0002-8282-469X
K. A. G. Olsen ⓘ https://orcid.org/0000-0002-7134-8296
A. Pieres ⓘ https://orcid.org/0000-0001-9186-6042
J. D. Sakowska ⓘ https://orcid.org/0000-0002-1594-1466
J. D. Simon ⓘ https://orcid.org/0000-0002-4733-4994
G. S. Stringfellow ⓘ https://orcid.org/0000-0003-1479-3059
E. J. Tollerud ⓘ https://orcid.org/0000-0002-9599-310X
A. K. Vivas ⓘ https://orcid.org/0000-0003-4341-6172
A. R. Walker ⓘ https://orcid.org/0000-0002-7123-8943
R. H. Wechsler ⓘ https://orcid.org/0000-0003-2229-011X

References

Aihara, H., Arimoto, N., Armstrong, R., et al. 2018, PASJ, 70, S4
Astropy Collaboration, Robitaille, T. P., Tollerud, E. J., et al. 2013, A&A, 558, A33
Balbinot, E., Santiago, B. X., da Costa, L., et al. 2013, ApJ, 767, 101
Barbary, K. 2016, JOSS, 1, 58
Battaglia, G., Taibi, S., Thomas, G. F., & Fritz, T. K. 2022, A&A, 657, A54
Baumgardt, H., Faller, J., Meinhold, N., McGovern-Greco, C., & Hilker, M. 2022, MNRAS, 510, 3531
Bechtol, K., Drlica-Wagner, A., Balbinot, E., et al. 2015, ApJ, 807, 50
Bell, E. F., Smercina, A., Price, P. A., et al. 2022, ApJL, 937, L3
Bellazzini, M., Ferraro, F. R., & Ibata, R. 2003, AJ, 125, 188
Blumenthal, G. R., Faber, S. M., Primack, J. R., & Rees, M. J. 1984, Natur, 311, 517
Bovill, M. S., & Ricotti, M. 2009, ApJ, 693, 1859
Bressan, A., Marigo, P., Girardi, L., et al. 2012, MNRAS, 427, 127
Brown, T. M., Tumlinson, J., Geha, M., et al. 2014, ApJ, 796, 91
Cantu, S. A., Pace, A. B., Marshall, J., et al. 2021, ApJ, 916, 81
Carlin, J. L., Sand, D. J., Muñoz, R. R., et al. 2017, AJ, 154, 267
Cerny, W., Pace, A. B., Drlica-Wagner, A., et al. 2021a, ApJL, 920, L44
Cerny, W., Pace, A. B., Drlica-Wagner, A., et al. 2021b, ApJ, 910, 18
Cerny, W., Simon, J. D., Li, T. S., et al. 2023, ApJ, 942, 111
Chabrier, G. 2003, PASP, 115, 763
Chambers, K. C., Magnier, E. A., Metcalfe, N., et al. 2016, arXiv:1612.05560
Chaussidon, E., Yèche, C., Palanque-Delabrouille, N., et al. 2023, ApJ, 944, 107
Coleman, M. G., de Jong, J. T. A., Martin, N. F., et al. 2007, ApJL, 668, L43
Collins, M. L. M., Charles, E. J. E., Martínez-Delgado, D., et al. 2022, MNRAS, 515, L72
Conn, B. C., Jerjen, H., Kim, D., & Schirmer, M. 2018a, ApJ, 852, 68
Conn, B. C., Jerjen, H., Kim, D., & Schirmer, M. 2018b, ApJ, 857, 70
Da Costa, G. S., & Armandroff, T. E. 1995, AJ, 109, 2533
Darragh-Ford, E., Nadler, E. O., McLaughlin, S., & Wechsler, R. H. 2021, ApJ, 915, 48
Davies, R. L., Allington-Smith, J. R., Bettess, P., et al. 1997, Proc. SPIE, 2871, 1099
Demortier, L., & Lyons, L. 2002, Technical Report 5776, CDF/ANAL/PUBLIC/5776
DES Collaboration 2005, arXiv:astro-ph/0510346
DES Collaboration, Abbott, T. M. C., Abdalla, F. B., et al. 2018, ApJS, 239, 18
DES Collaboration, Abbott, T. M. C., Adamów, M., et al. 2021, ApJS, 255, 20
Dey, A., Schlegel, D. J., Lang, D., et al. 2019, AJ, 157, 168
Diemand, J., Kuhlen, M., & Madau, P. 2007, ApJ, 667, 859
Drlica-Wagner, A., Bechtol, K., Mau, S., et al. 2020, ApJ, 893, 47
Drlica-Wagner, A., Bechtol, K., Rykoff, E. S., et al. 2015, ApJ, 813, 109
Drlica-Wagner, A., Carlin, J. L., Nidever, D. L., et al. 2020, ApJS, 256, 2
Drlica-Wagner, A., Ferguson, P. S., Adamów, M., et al. 2022, ApJS, 261, 38
Erkal, D., & Belokurov, V. A. 2020, MNRAS, 495, 2554
Fadely, R., Willman, B., Geha, M., et al. 2011, AJ, 142, 88
Flaugher, B. L., Abbott, T. M. C., Annis, J., et al. 2010, Proc. SPIE, 7735, 77350D
Forbes, D. A., & Bridges, T. 2010, MNRAS, 404, 1203
Foreman-Mackey, D., Hogg, D. W., Lang, D., & Goodman, J. 2013, PASP, 125, 306
Frebel, A., & Bromm, V. 2012, ApJ, 759, 115
Fritz, T. K., Battaglia, G., Pawlowski, M. S., et al. 2018, A&A, 619, A103
Fritz, T. K., Carrera, R., Battaglia, G., & Taibi, S. 2019, A&A, 623, A129
Gaia Collaboration, Brown, A. G. A., Vallenari, A., et al. 2021, A&A, 649, A1
Garro, E. R., Minniti, D., Gómez, M., & Alonso-García, J. 2021, A&A, 654, A23
Górski, K. M., Hivon, E., Banday, A. J., et al. 2005, ApJ, 622, 759
Griffen, B. F., Ji, A. P., Dooley, G. A., et al. 2016, ApJ, 818, 10
Hargis, J. R., Willman, B., & Peter, A. H. G. 2014, ApJL, 795, L13
Harris, W. E. 1996, AJ, 112, 1487
Hidalgo, S. L., Pietrinferni, A., Cassisi, S., et al. 2018, ApJ, 856, 125
Homma, D., Chiba, M., Komiyama, Y., et al. 2019, PASJ, 71, 94
Homma, D., Chiba, M., Okamoto, S., et al. 2016, ApJ, 832, 21
Hook, I. M., Jørgensen, I., Allington-Smith, J. R., et al. 2004, PASP, 116, 425
Hunter, J. D. 2007, CSE, 9, 90
Ibata, R. A., Gilmore, G., & Irwin, M. J. 1994, Natur, 370, 194
Jenkins, A., Frenk, C. S., White, S. D. M., et al. 2001, MNRAS, 321, 372
Jethwa, P., Erkal, D., & Belokurov, V. 2016, MNRAS, 461, 2212
Ji, A. P., Li, T. S., Simon, J. D., et al. 2020, ApJ, 889, 27
Ji, A. P., Simon, J. D., Frebel, A., Venn, K. A., & Hansen, T. T. 2019, ApJ, 870, 83
Jones, E., Oliphant, T., Peterson, P., et al. 2001, SciPy: Open Source Scientific Tools for Python, http://www.scipy.org/
Ivezić, Ž., Kahn, S. M., Tyson, J. A., et al. 2019, ApJ, 873, 111
Kallivayalil, N., Sales, L. V., Zivick, P., et al. 2018, ApJ, 867, 19
Kim, D., & Jerjen, H. 2015, ApJ, 799, 73
Koposov, S. E., Belokurov, V., & Torrealba, G. 2017, MNRAS, 470, 2702
Koposov, S. E., Belokurov, V., Torrealba, G., & Evans, N. W. 2015, ApJ, 805, 130
Kravtsov, A. 2010, AdAst, 2010, 281913
Labrie, K., Anderson, K., Cárdenes, R., Simpson, C., & Turner, J. E. H. 2019, in ASP Conf. Ser. 523, Astronomical Data Analysis Software and Systems XXVII, ed. P. J. Teuben et al. (San Francisco, CA: ASP), 321
Laevens, B. P. M., Martin, N. F., Bernard, E. J., et al. 2015, ApJ, 813, 44
Law, D. R., & Majewski, S. R. 2010a, ApJ, 718, 1128
Law, D. R., & Majewski, S. R. 2010b, ApJ, 714, 229
Li, H., Hammer, F., Babusiaux, C., et al. 2021, ApJ, 916, 8
Li, T. S., Simon, J. D., Kuehn, K., et al. 2018a, ApJ, 866, 22
Li, T. S., Simon, J. D., Pace, A. B., et al. 2018b, ApJ, 857, 145
Lindegren, L., Klioner, S. A., Hernández, J., et al. 2021, A&A, 649, A2
Longeard, N., Martin, N., Ibata, R. A., et al. 2021, MNRAS, 503, 2754
Longeard, N., Martin, N., Starkenburg, E., et al. 2018, MNRAS, 480, 2609
Longeard, N., Martin, N., Starkenburg, E., et al. 2020, MNRAS, 491, 356
Luque, E., Pieres, A., Santiago, B., et al. 2017, MNRAS, 468, 97
Manwadkar, V., & Kravtsov, A. V. 2022, MNRAS, 516, 3944
Martin, N. F., de Jong, J. T. A., & Rix, H.-W. 2008, ApJ, 684, 1075
Martínez-Delgado, D., Karim, N., Charles, E. J. E., et al. 2022, MNRAS, 509, 16
Martínez-Vázquez, C. E., Salinas, R., & Vivas, A. K. 2021, AJ, 161, 120

Mau, S., Cerny, W., Pace, A. B., et al. 2020, ApJ, 890, 136
McConnachie, A. W. 2012, AJ, 144, 4
McConnachie, A. W., & Venn, K. A. 2020, AJ, 160, 124
Meylan, G., & Heggie, D. C. 1997, A&ARv, 8, 1
Monelli, M., Hidalgo, S. L., Stetson, P. B., et al. 2010, ApJ, 720, 1225
Morganson, E., Gruendl, R. A., Menanteau, F., et al. 2018, PASP, 130, 074501
Muñoz, R. R., Côté, P., Santana, F. A., et al. 2018, ApJ, 860, 66
Muñoz, R. R., Geha, M., Côté, P., et al. 2012, ApJL, 753, L15
Mutlu-Pakdil, B., Sand, D. J., Carlin, J. L., et al. 2018, ApJ, 863, 25
Mutlu-Pakdil, B., Sand, D. J., Crnojević, D., et al. 2020, ApJ, 902, 106
Mutlu-Pakdil, B., Sand, D. J., Crnojević, D., et al. 2022, ApJ, 926, 77
Mutlu-Pakdil, B., Sand, D. J., Walker, M. G., et al. 2019, ApJ, 885, 53
Nadler, E. O., Mao, Y.-Y., Green, G. M., & Wechsler, R. H. 2019, ApJ, 873, 34
Pace, A. B., Erkal, D., & Li, T. S. 2022, ApJ, 940, 136
Pace, A. B., & Li, T. S. 2019, ApJ, 875, 77
Patel, E., Kallivayalil, N., Garavito-Camargo, N., et al. 2020, ApJ, 893, 121
Pawlowski, M. S., & Kroupa, P. 2013, MNRAS, 435, 2116
Pawlowski, M. S., & Kroupa, P. 2020, MNRAS, 491, 3042
Pawlowski, M. S., Pflamm-Altenburg, J., & Kroupa, P. 2012, MNRAS, 423, 1109
Pietrinferni, A., Hidalgo, S., Cassisi, S., et al. 2021, ApJ, 908, 102
Plummer, H. C. 1911, MNRAS, 71, 460
Price-Whelan, A. M. 2017, JOSS, 2, 388
Price-Whelan, A. M., Sipőcz, B. M., Günther, H. M., et al. 2018, AJ, 156, 123
Raichoor, A., Moustakas, J., Newman, J. A., et al. 2023, AJ, 165, 126
Riley, A. H., & Strigari, L. E. 2020, MNRAS, 494, 983
Sacchi, E., Richstein, H., Kallivayalil, N., et al. 2021, ApJL, 920, L19
Sales, L. V., Navarro, J. F., Kallivayalil, N., & Frenk, C. S. 2017, MNRAS, 465, 1879
Sand, D. J., Mutlu-Pakdil, B., Jones, M. G., et al. 2022, ApJL, 935, L17
Sand, D. J., Seth, A., Olszewski, E. W., et al. 2010, ApJ, 718, 530
Sand, D. J., Strader, J., Willman, B., et al. 2012, ApJ, 756, 79
Schlafly, E. F., & Finkbeiner, D. P. 2011, ApJ, 737, 103
Schlegel, D. J., Finkbeiner, D. P., & Davis, M. 1998, ApJ, 500, 525
Searle, L., & Zinn, R. 1978, ApJ, 225, 357
Shanks, T., Metcalfe, N., Chehade, B., et al. 2015, MNRAS, 451, 4238
Simon, J. D. 2019, ARA&A, 57, 375
Simon, J. D., Brown, T. M., Drlica-Wagner, A., et al. 2021, ApJ, 908, 18
Simon, J. D., Li, T. S., Erkal, D., et al. 2020, ApJ, 892, 137
Smith, S. E. T., Jensen, J., Roediger, J., et al. 2022, arXiv:2209.08242
Springel, V., Wang, J., Vogelsberger, M., et al. 2008, MNRAS, 391, 1685
Stetson, P. B. 1987, PASP, 99, 191
Torrealba, G., Belokurov, V., Koposov, S. E., et al. 2018, MNRAS, 475, 5085
Torrealba, G., Belokurov, V., & Koposov, S. E. 2019a, MNRAS, 484, 2181
Torrealba, G., Belokurov, V., Koposov, S. E., et al. 2019b, MNRAS, 488, 2743
van der Walt, S., Colbert, S. C., & Varoquaux, G. 2011, CSE, 13, 22
Vasiliev, E., Belokurov, V., & Erkal, D. 2021, MNRAS, 501, 2279
White, S. D. M., & Rees, M. J. 1978, MNRAS, 183, 341
Willman, B., Blanton, M. R., West, A. A., et al. 2005, AJ, 129, 2692
Willman, B., Geha, M., Strader, J., et al. 2011, AJ, 142, 128
Willman, B., & Strader, J. 2012, AJ, 144, 76
York, D. G., Adelman, J., Anderson, J. E. J., et al. 2000, AJ, 120, 1579
Zonca, A., Singer, L., Lenz, D., et al. 2019, JOSS, 4, 1298